applied sciences

MDPI

Article

Active Support System for the Correction of a 4m SiC Primary Mirror Based on the Bending Mode

Zhiyuan Yu [1,2,*], Xiaoxia Wu [1] and Fuguo Wang [1]

[1] Changchun Institute of Optics, Fine Mechanics and Physics, Chinese Academy of Sciences, Changchun 130033, China; wuxiaoxia@ciomp.ac.cn (X.W.); wangfuguo@ciomp.ac.cn (F.W.)
[2] University of Chinese Academy of Sciences, Beijing 100049, China
* Correspondence: yuzhiyuan18@mails.ucas.edu.cn

Abstract: Active optics is a key technology in ground-based large-aperture telescopes. The active correction of the surface shape of the primary mirror is used to reduce the surface shape error and improve the imaging quality. At present, the structure of the active optics support system is not standardized. Therefore, to ensure the imaging quality of a telescope using a 4m SiC (silicon carbide) primary mirror, this article designed an active support system for the primary mirror and comprehensively evaluated the performance of the system. The system used pneumatic actuators to correct the surface shape of the primary mirror and a six-hardpoint positioning mechanism to correct the pose of the primary mirror. A method for compensating for the force on the hardpoints that causes protrusions and dents on the primary mirror surface was proposed, which effectively improved the accuracy of the primary mirror surface. The bending-mode method was used to determine the correction force. To achieve better results in the surface shape correction based on the bending mode, the relationship between the order of the bending modes used in the correction and the correction effect was studied, enabling the system to achieve a higher surface shape accuracy with a smaller correction force. Finally, the performance of the system was evaluated under various conditions, such as under gravity, thermal load, and wind load. The results indicated that the system had good correction effects on the deformation of the primary mirror under various operating conditions and could meet the requirements of optical design for surface accuracy. In conclusion, this study not only verified the application of active optics technology based on the bending mode in large-aperture SiC mirrors, but also improved on the relevant theoretical research on active optics.

Keywords: active optics; primary mirror support; six-hardpoint positioning mechanism; force on hardpoint; bending mode

check for updates

Citation: Yu, Z.; Wu, X.; Wang, F. Active Support System for the Correction of a 4m SiC Primary Mirror Based on the Bending Mode. *Appl. Sci.* **2023**, *13*, 9966. https://doi.org/10.3390/app13179966

Academic Editor: Daomu Zhao

Received: 6 August 2023
Revised: 29 August 2023
Accepted: 30 August 2023
Published: 4 September 2023

1. Introduction

The support system of the primary mirror is a key system in ground-based large-aperture telescopes, as it determines the surface shape and pose accuracy of the primary mirror and plays a decisive role in the imaging quality of the telescope. The primary mirror support system must resist the influence of gravity, thermal load, and wind load, which are often dynamic. Therefore, active optics has been proposed and applied. Since its first application to the New Technology Telescope (NTT) at the European Southern Observatory, active optics technology has become a key technology for large-aperture telescopes. Active optics refers to the active correction of the surface shape of the primary mirror, which can significantly reduce the surface shape error caused by various loads and improve the imaging quality and observation performance of the telescope [1–4]. It can achieve the closed-loop control of the surface shape of the primary mirror, providing feedback through the monitoring of the primary mirror shape and adjusting and correcting the primary mirror shape through the use of actuators [5,6].

The active support system based on active optics technology has two subsystems, the surface control system and the positioning system. The surface control system uses proper force actuators to output axial force to the primary mirror to correct the surface shape, and the positioning system is used to constrain the rigid displacement of the primary mirror relative to the mirror cell. Active optics technology is currently applied to more than ten telescopes, which can be divided into three categories according to the positioning system scheme. The first type uses fixed positioning points to achieve primary mirror positioning and includes the NTT [7], VLT Survey Telescope (VST) [8], Subaru Telescope [9], and Southern Astrophysical Research Telescope (SOAR) [10]. The second type uses virtual positioning points and includes the Advanced Electro-Optical System 3.6 m telescope (AEOS) [11], Very Large Telescope (VLT) [12], and Gemini Telescope [13]. The third type uses a six-hardpoint positioning mechanism for primary mirror positioning, including the MMT Telescope [14], Large Binocular Telescope (LBT) [15,16], and the unfinished Large Synoptic Survey Telescope (LSST) [17,18]. Although a rough classification is possible, the structure of the active support system and primary mirror are not standardized, and each support system is customized for the specific telescope and primary mirror [19]. Therefore, in order to ensure the surface accuracy of a 4m SiC lightweight primary mirror, this article designs an active support system for the primary mirror. Considering that primary mirror positioning based on hardpoints can maintain and adjust the pose of the primary mirror, the designed system uses hardpoints for primary mirror positioning.

The optical design of the telescope requires the active support system for the 4m SiC primary mirror to ensure a root mean square (rms) of the primary mirror shape error of less than $\lambda/30$ (λ = 632.8 nm). The designed system uses pneumatic actuators for conducting surface corrections and to also provide force to support the gravity of the primary mirror. Some studies have shown that there is mutual interference between the surface control system and the positioning system. For example, Li et al. [20] studied the interference of fixed points in surface shape correction and proposed using compensation planes to solve it and achieved a good surface shape. However, there is currently no research to solve the problem of reduced surface accuracy caused by force on hardpoints. Therefore, a method is proposed to compensate for the force on the hardpoints, which solves the problem of protrusions and dents on the primary mirror surface caused by the force on the hardpoints.

In order to achieve closed-loop control of the primary mirror surface shape, the required correction force must be calculated based on the primary mirror shape error. Currently, four methods are used to calculate the correction force. The free-resonance method establishes a mapping relationship between the free-resonance modes of the primary mirror and the correction force. Then, the free-resonance modes are used to fit the surface error of the primary mirror, thereby determining the correction force [21,22]. This method is generally applied to thin primary mirrors rather than lightweight honeycomb mirrors. The second method, called the direct least squares method, establishes a mapping relationship between the force and deformation of the primary mirror surface through an interaction matrix, thereby determining the correction force [23]. The correction force obtained with this method is typically relatively large. The third method, called damped least squares or constrained least squares, is an improvement on the direct least squares method, which introduces damping factors to limit the amplitude of the correction force [24]. This method is relatively complex and requires optimization to obtain the optimal damping factors. The fourth method, called the bending-mode method, generates several bending modes through the singular value decomposition (SVD) of the interaction matrix. Then, the primary mirror surface shape error is fitted with several lower-order bending modes, thereby determining the correction force [25]. Considering that the bending-mode method avoids the problems of the first three methods, we use this method to solve the correction force. However, current research on bending modes [25–27] has ignored the issue of how to reasonably select the orders of bending modes. Therefore, this article investigates the relationship between the orders of bending modes used in surface shape correction and the correction effect, enabling the system to achieve a higher primary mirror surface shape accuracy with a smaller correction force.

The main contributions and innovations of this article are as follows: (1) The design and performance evaluation of an active support system for a 4m SiC primary mirror is achieved and the system can achieve good surface accuracy. (2) A method for compensating for the force on the hardpoints is proposed to solve the problem of protrusions and dents on the primary mirror surface caused by the force on hardpoints. (3) The bending-mode method is deeply studied, the relationship between the order of the bending modes used in the surface shape correction and the correction effect is investigated, and the active optics correction method based on the bending mode is improved.

The remainder of this article is organized as follows: Section 2 explains the principle and structure of the designed 4m SiC primary mirror active support system. Section 3 discusses the surface and pose correction methods for the mirror and proposes a compensation method for the force on the hardpoints. Section 4 evaluates the performance of the designed system and tests its performance under conditions such as gravity, thermal load, and wind load. Section 5 provides the conclusion.

2. Principle and Structural Design of the Active Support System for a 4m SiC Primary Mirror

The active support system for a 4m SiC primary mirror is shown in Figure 1. The system used pneumatic surface control actuators and a six-hardpoint positioning mechanism to connect the primary mirror and mirror cell. The actuators and hardpoints were epoxy-bonded to the backface of the primary mirror, and the bonding position was determined with a laser tracker. The pneumatic actuators were used to correct the surface shape of the primary mirror and the six-hardpoint positioning mechanism was used to define the relative pose of the primary mirror and mirror cell. The primary mirror was a lightweight mirror weighing 1600 kg, with a diameter of 4 m and center hole diameter of 0.5 m. It was composed of SiC and had the structure of a semienclosed honeycomb. The primary mirror had a surface thickness of 15 mm and radial and circumferential rib plates arranged on its back, forming numerous fan-shaped lightweight holes. The rib plate thickness was 7 mm (some rib plates were 12 mm thick).

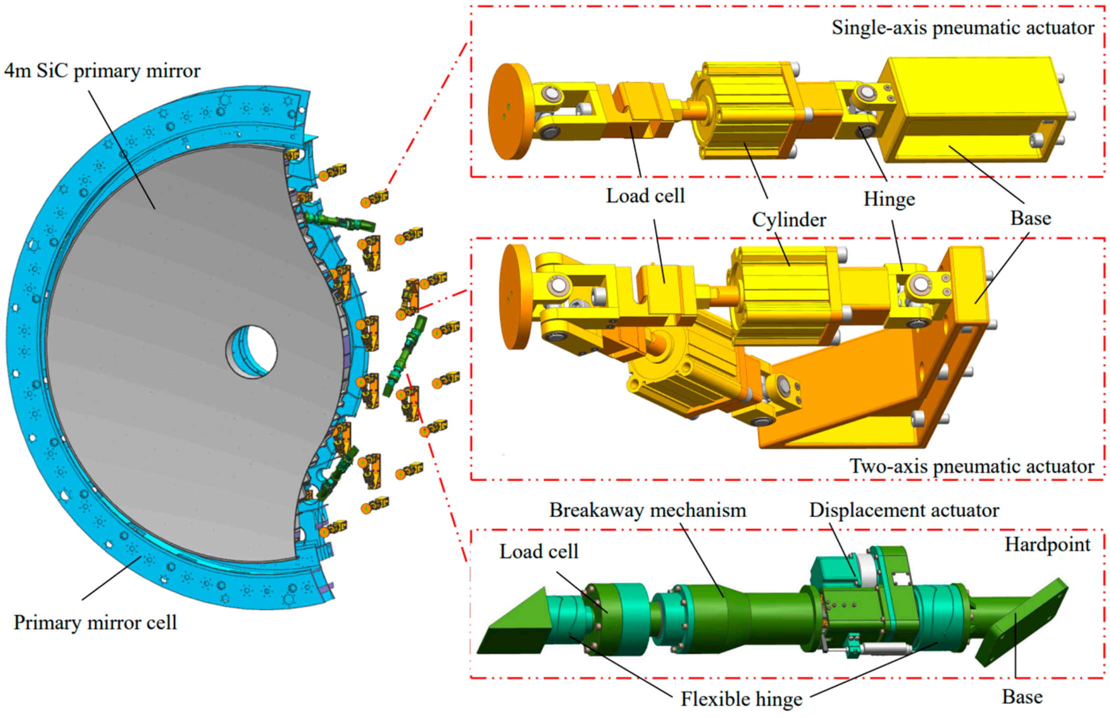

Figure 1. Structural schematic of the active support system for a 4m SiC primary mirror.

2.1. Pneumatic Surface Control Actuators and Hardpoints

The pneumatic surface control actuators correct the surface shape of the primary mirror and support its weight. It is structurally divided into single- and two-axis actuators. Single-axis actuators provide only axial force, whereas two-axis actuators provide both axial and radial forces.

A total of 54 pneumatic surface control actuators were installed at 54 support points on the back of the primary mirror. The positions of the support points were obtained through a finite element analysis and optimization, and their positions and numbers are shown in Figure 2. The origin of the coordinate system shown in Figure 2 coincided with the vertex of the reflecting surface of the primary mirror. The y-axis was parallel to the elevation axis, the unmarked z-axis was parallel to the optical axis and pointed to the observation target, and the x-axis direction was determined using the right-hand rule. Among the 30 two-axis actuators, 26 were arranged parallel to the x-axis and could output a radial force in the x-direction to balance the radial component of gravity. The two-axis actuators 19, 24, 25, and 30 were arranged in the y-axis direction and could output a radial force in the y-direction. The structures of the single- and two-axis actuators were as shown in Figure 1.

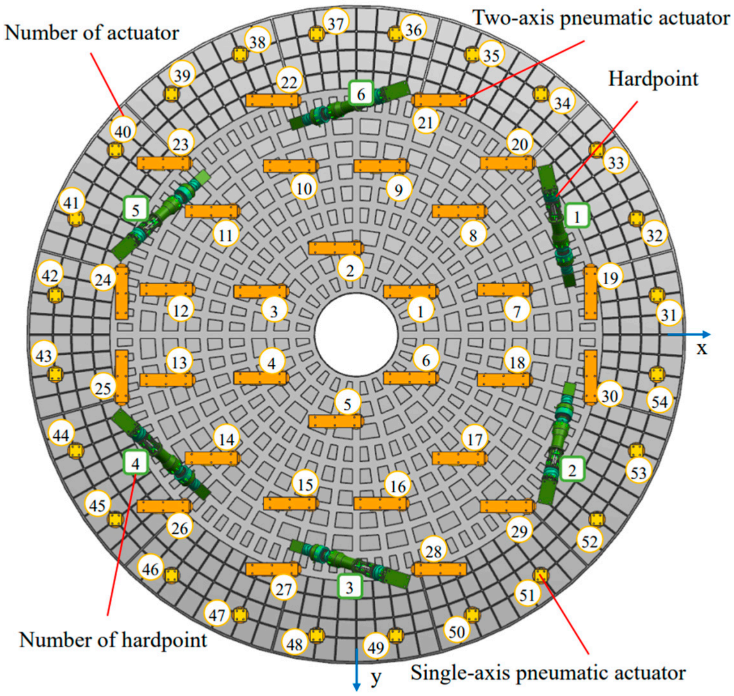

Figure 2. Layout and numbering of pneumatic surface control actuators and hardpoints.

The actuator was powered with a cylinder. The stroke of the cylinder was ±20 mm and the output force range was ±0.85 kN. The range of the output force of the single-axis actuator was the same as that of the cylinder. The range of the axial force output by the two-axis actuator was ±1.45 kN, and the range of radial force was ±0.85 kN. Each cylinder was connected in series with two hinges, enabling the pneumatic actuator to meet the displacement of ±20 mm and rotation of ±0.21° of the primary mirror. The range of motion of the mirror was obtained through a kinematic analysis based on the Monte Carlo method. Each cylinder was connected in series with an S-type tension and pressure sensor that could achieve closed-loop control of the output force.

Six hardpoints with the same structure formed a six-hardpoint positioning mechanism, which was used to define the relative pose between the primary mirror and mirror cell. The numbering of the hardpoints is illustrated in Figure 2. The hardpoints can be understood as linear displacement actuators with a high axial stiffness, as shown in Figure 1. The six-hardpoint positioning mechanism adjusted the pose of the primary mirror by changing the length of the hardpoints. Maintaining the length of the hardpoints unchanged could preserve the pose of the primary mirror. The flexible hinges in the hardpoints provided the necessary degrees of freedom, and a breakaway mechanism provided an overload protection function. A spoke-type tension and pressure sensor measured the force on the hardpoints. The axial stiffness of the hardpoints, 33.044 N/µm, could provide a one-order natural frequency of over 25 Hz for the system [28]. The displacement accuracy of the hardpoints depended on the displacement accuracy of the actuator. The displacement stroke of the hardpoints was ±10 mm, and the displacement resolution was 0.33 µm. The repeatability accuracy was 7.026 µm.

2.2. Finite Element Model of the Active Support System for the 4m SiC Primary Mirror

A finite element model of the primary mirror support system was established, as shown in Figure 3. To improve the efficiency of the analysis, the hardpoints were simplified as rod structures in the model, the rod element was used, and the axial stiffness was set to 33 N/µm. Gravity counter forces and correction forces were applied at the 54 support points to simulate the force actuator. The primary mirror was composed of SiC, and the mirror cell was composed of carbon structural steel Q235. The model contained 309,433 units and 893,116 nodes.

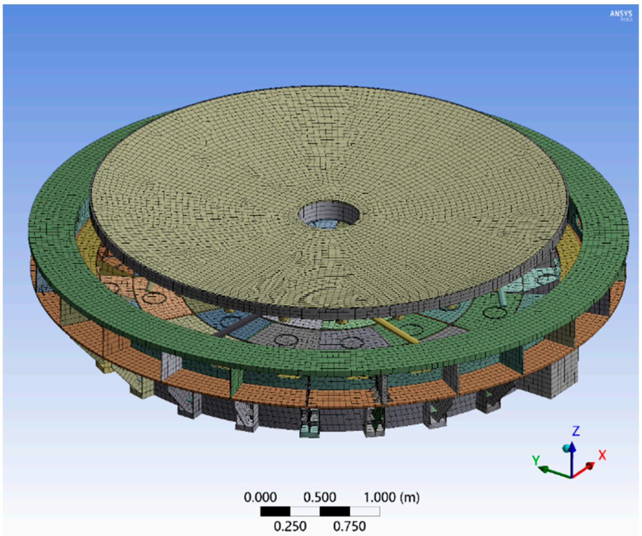

Figure 3. Finite element model of the active support system for the 4m SiC primary mirror.

3. Active Optics Correction of the 4m SiC Primary Mirror

The main purpose of the active support system is to ensure the surface shape and pose accuracy of the primary mirror, thereby ensuring a good imaging quality of the telescope. Therefore, active optics includes two parts: the primary mirror shape and pose corrections. This section introduces the correction methods and discusses the relevant mathematical derivation. In addition, to ensure the accuracy of the surface shape and pose, a method for compensating for the force on the hardpoints was proposed.

3.1. Surface Shape Correction of the 4m SiC Primary Mirror

3.1.1. Principle of Surface Shape Correction Based on the Bending Mode

A surface shape correction requires force actuators to output axial forces to the primary mirror. Therefore, the key to surface correction is the calculation of the correction force, which is based on measuring the surface error of the primary mirror. The designed active support system for the 4m SiC primary mirror used the bending-mode method to calculate the correction force.

According to Hooke's law, the relationship between the deformation of the primary mirror and the force is linear [20]. Therefore, if we could determine the surface deformation $\boldsymbol{A}_i$ after applying the axial unit force to each support point and obtain the interaction matrix $\boldsymbol{A} = [\boldsymbol{A}_1, \boldsymbol{A}_2, \ldots, \boldsymbol{A}_{54}]$, we could obtain the relationship between the force and deformation of the primary mirror, where i represents the serial number of the support point. $\boldsymbol{A}_i$ is called the influence function of the unit force and is a column vector of length m, where m is the number of sampling points for the primary mirror shape, requiring $m > 54$. For a set of forces $\boldsymbol{F}$ applied to the support points, the resulting deformation of the primary mirror surface $\boldsymbol{W}$ satisfied

$$\boldsymbol{W} = \boldsymbol{AF} = \sum_{i=1}^{54} \boldsymbol{A}_i F_i \tag{1}$$

where F_i is the i-th element of vector $\boldsymbol{F}$. The mapping relationship between the force acting on the primary mirror and the deformation of the mirror surface was established based on the interaction matrix $\boldsymbol{A}$. The correction force could be determined using Equation (1). The above method is the direct least squares method. However, the correction force obtained using this method is often extremely high, because the method attempts to correct all low- and high-order components in the primary mirror shape error, and correcting higher-order aberrations would result in a large correction force, which may exceed the output force threshold of the force actuator and may also damage the primary mirror. In addition, the shape error of the primary mirror is often dominated by low-order aberrations, and correcting high-frequency aberrations results in a very small improvement in the shape. Therefore, the benefits of this method are limited.

The fundamental flaw of this method is that the influence function $\boldsymbol{A}_i$ cannot reflect the difficulty of the surface shape correction. Therefore, excluding high-frequency components in surface shape errors is challenging. The bending-mode method can improve this situation. According to the principle of the method, SVD was performed on the interaction matrix $\boldsymbol{A}$:

$$\boldsymbol{A} = \boldsymbol{USV}^T \tag{2}$$

Then, the bending mode $\boldsymbol{B}_i$ and the bending-mode matrix $\boldsymbol{B}$ were obtained as follows:

$$\boldsymbol{B} = \begin{bmatrix} \boldsymbol{B}_1 & \boldsymbol{B}_2 & \cdots & \boldsymbol{B}_{54} \end{bmatrix} = \boldsymbol{U} = \boldsymbol{AVS}^{-1} \tag{3}$$

where

$$\boldsymbol{V} = \begin{bmatrix} \boldsymbol{V}_1 & \boldsymbol{V}_2 & \cdots & \boldsymbol{V}_{54} \end{bmatrix} \tag{4}$$

$$\boldsymbol{B}_i = \boldsymbol{AV}_i \frac{1}{\mu_i} \tag{5}$$

where μ_i is the element in matrix $\boldsymbol{S}$ and the singular value that affects matrix $\boldsymbol{A}$. By introducing the bending mode $\boldsymbol{B}_i$ into Equation (1), the required force $\boldsymbol{F}_{Bi}$ for $\boldsymbol{B}_i$ could be calculated as follows:

$$\boldsymbol{W} = \boldsymbol{B}_i = \boldsymbol{AV}_i \frac{1}{\mu_i} = \boldsymbol{AF}_{Bi} \tag{6}$$

$$\boldsymbol{F}_{Bi} = \boldsymbol{V}_i \frac{1}{\mu_i} \tag{7}$$

where $\boldsymbol{F}_{Bi}$, known as the bending-mode force, is the force required to generate the surface $\boldsymbol{B}_i$. Combining $\boldsymbol{F}_{Bi}$ into the bending-mode force matrix $\boldsymbol{F}_B$,

$$\boldsymbol{F}_B = \begin{bmatrix} \boldsymbol{F}_{B1} & \boldsymbol{F}_{B2} & \cdots & \boldsymbol{F}_{B54} \end{bmatrix} \tag{8}$$

The bending-mode method used $\boldsymbol{B}_i$ to fit the primary mirror shape $\boldsymbol{W}$ and then solved for the correction force:

$$\boldsymbol{W} = \sum_{i=1}^{54} \boldsymbol{B}_i b_i \tag{9}$$

The fitting result was the fitting coefficient b_i, which was the proportion of each bending mode $\boldsymbol{B}_i$ to the primary mirror shape $\boldsymbol{W}$. If we multiplied and summed b_i with the bending-mode force $\boldsymbol{F}_{Bi}$, we obtained the required force $\boldsymbol{F}$ for $\boldsymbol{W}$:

$$\boldsymbol{F} = \sum_{i=1}^{54} \boldsymbol{F}_{Bi} b_i = \boldsymbol{F}_B \begin{bmatrix} b_1 & b_2 & \cdots & b_{54} \end{bmatrix}^T \tag{10}$$

The advantage of the bending-mode method is that the stiffness of $\boldsymbol{B}_i$ increased with the order. According to the SVD properties, the rms of all $\boldsymbol{B}_i$ was equal, and the rms of all $\boldsymbol{V}_i$ was equal. As i increased, the value of μ_i gradually decreased. Therefore, according to Equation (7), $\boldsymbol{F}_{Bi}$ gradually increased. This indicated that the stiffness and frequency of $\boldsymbol{B}_i$ gradually increased with increasing i. Therefore, if only a few low-order bending modes $\boldsymbol{B}_i$ were used to fit $\boldsymbol{W}$, the amplitude of the correction force could be effectively suppressed. In addition, owing to the dominant role of low-order aberrations in the surface error, this method could ensure a good surface correction effect and achieve an accurate surface shape.

Owing to the standard orthogonality among $\boldsymbol{B}_i$, when fitting with the first q orders of $\boldsymbol{B}_i$, only the first q term of b_i had to be retained, and the other terms had to be set to zero. The solution method for the correction force was

$$\boldsymbol{F} = \boldsymbol{F}_B \begin{bmatrix} b_1 & \cdots & b_q & 0 & \cdots & 0 \end{bmatrix}^T \tag{11}$$

3.1.2. Influence Function and Bending Mode of the 4m SiC Primary Mirror

The purpose of this section was to obtain the influence function, interaction matrix, and bending mode of the 4m SiC primary mirror based on the theory described in Section 3.1.1. To obtain the influence function $\boldsymbol{A}_i$ of the primary mirror, we used the equilibrium force $\boldsymbol{F}_{Ai}$ approximated using the unit force. The characteristic of $\boldsymbol{F}_{Ai}$ was that the force at the i-th support point was large, whereas that at the other support points was very small. The effect of $\boldsymbol{F}_{Ai}$ was similar to that of the unit force, except that the resultant force and moment of $\boldsymbol{F}_{Ai}$ on the primary mirror were zero, avoiding the trend of a rigid displacement of the primary mirror.

The 54 actuators were distributed across four concentric circles. Applying $\boldsymbol{F}_{Ai}$ sequentially to the primary mirror resulted in 54 influence functions $\boldsymbol{A}_i$. The influence functions and equilibrium forces are shown in Figure 4 (because of space limitations, only the influence functions corresponding to two actuators on each concentric circle were displayed; the surface shapes that were not provided were similar, owing to the symmetry of the structure).

Based on the 54 influence functions $\boldsymbol{A}_i$, we obtained the 4m SiC primary mirror interaction matrix $\boldsymbol{A}$. Then, SVD was performed on $\boldsymbol{A}$ to obtain the 54 bending modes $\boldsymbol{B}_i$ of the primary mirror (only the first 51 of the 54 modes were valid). As mentioned in Section 3.1.1, the rms values of all $\boldsymbol{B}_i$ were equal, and we further normalized them to 500 nm. Each $\boldsymbol{B}_i$ corresponded to a bending-mode force $\boldsymbol{F}_{Bi}$, as shown in Figure 5. The $\boldsymbol{B}_i$ in Figure 5 eliminated the tilt, and owing to space limitations, only the odd-order bending modes and forces in the first 20 orders were displayed. The bending modes in Figure 5 were derived from SVD, so they were the theoretical values of $\boldsymbol{B}_i$.

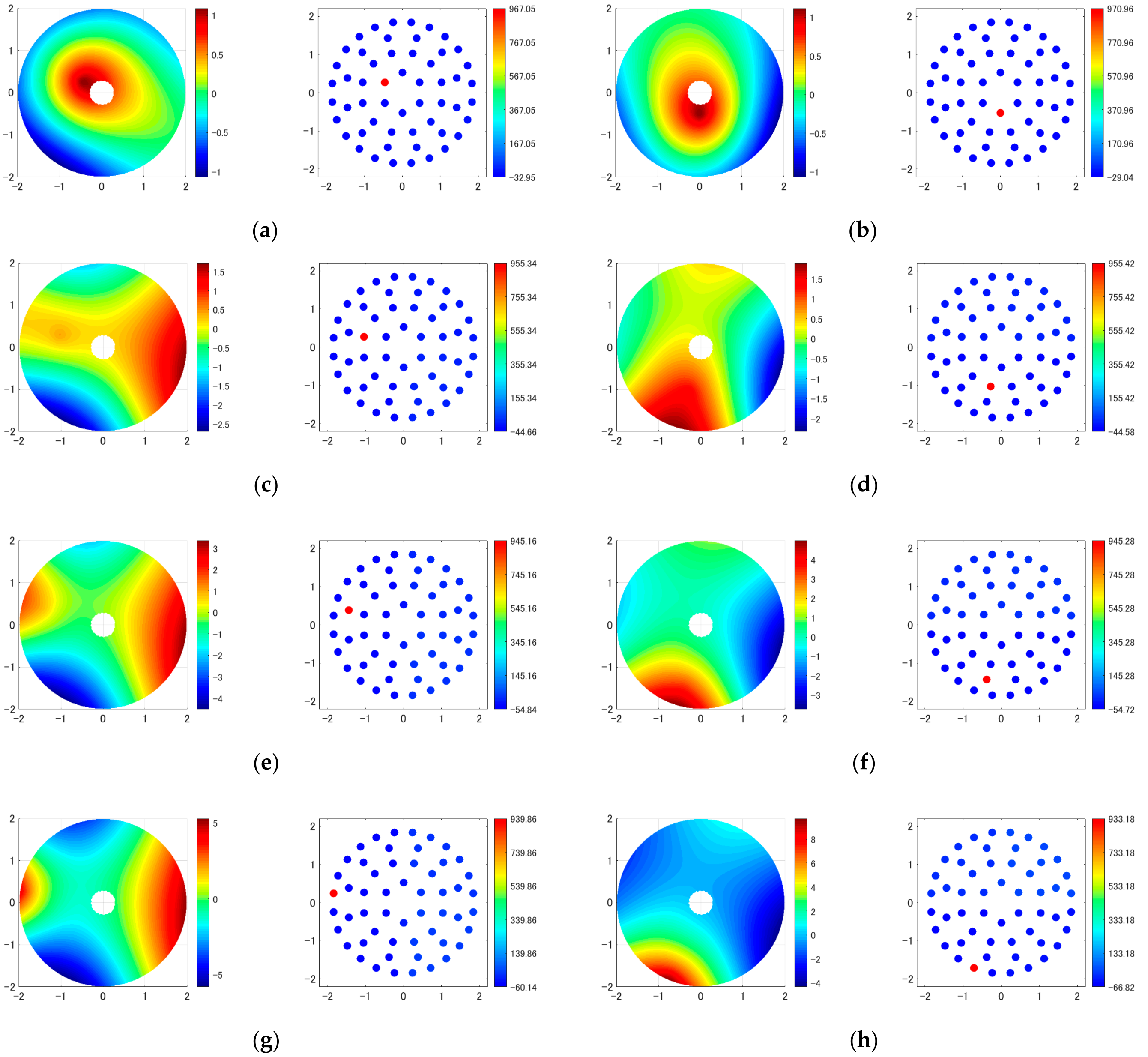

(**a**) (**b**)

(**c**) (**d**)

(**e**) (**f**)

(**g**) (**h**)

Figure 4. Influence function A_i and equilibrium force F_{Ai} of some pneumatic actuators. (**a**) Influence function A_1 and equilibrium force F_{A1}; (**b**) Influence function A_5 and equilibrium force F_{A5}; (**c**) Influence function A_7 and equilibrium force F_{A7}; (**d**) Influence function A_{16} and equilibrium force F_{A16}; (**e**) Influence function A_{19} and equilibrium force F_{A19}; (**f**) Influence function A_{28} and equilibrium force F_{A28}; (**g**) Influence function A_{31} and equilibrium force F_{A31}; (**h**) Influence function A_{50} and equilibrium force F_{A50}.

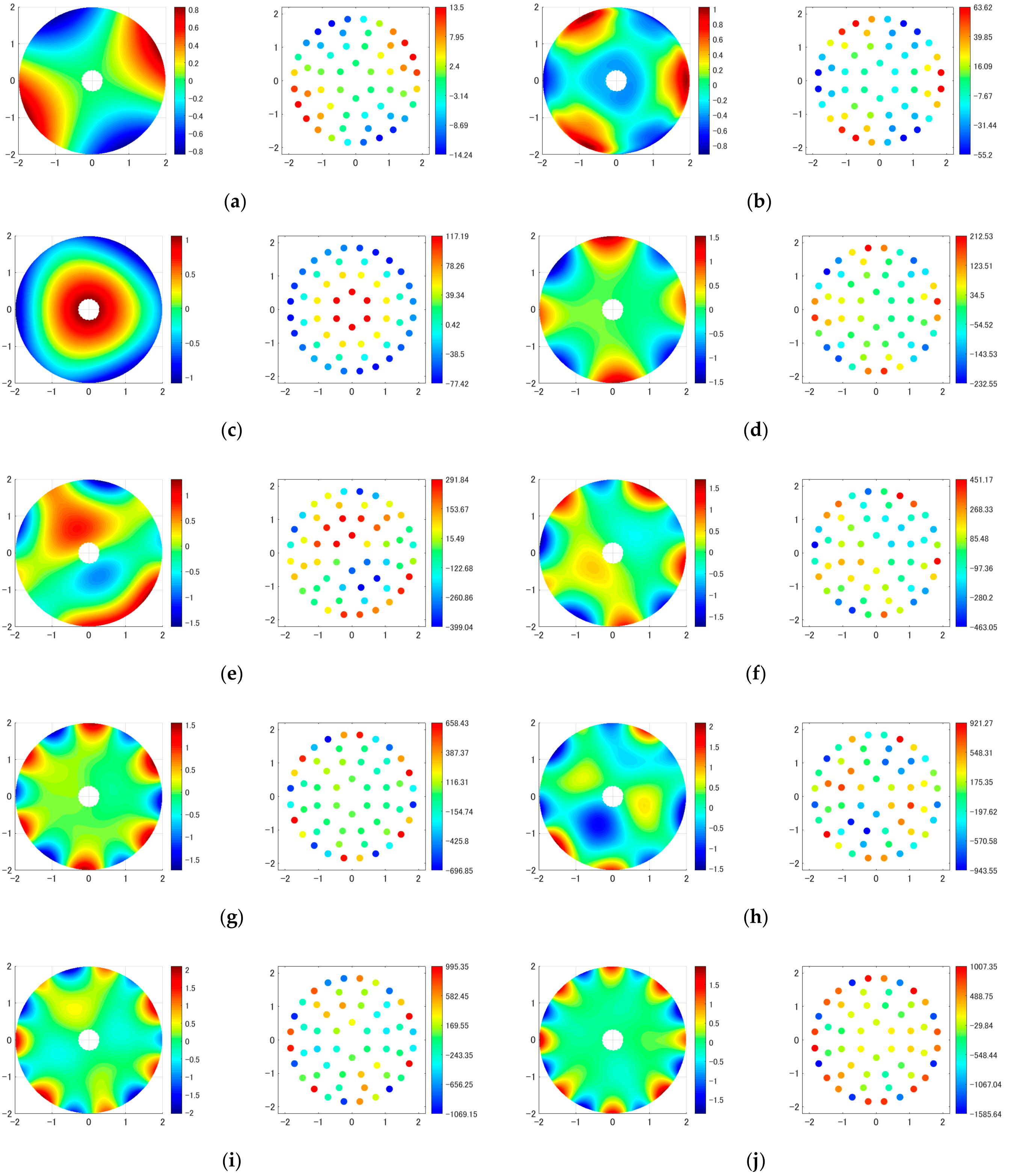

(**a**) (**b**)

(**c**) (**d**)

(**e**) (**f**)

(**g**) (**h**)

(**i**) (**j**)

Figure 5. Theoretical values of partial bending mode $\boldsymbol{B}_i$ of the 4m SiC primary mirror and corresponding bending-mode forces $\boldsymbol{F}_{Bi}$. (**a**) Bending mode $\boldsymbol{B}_1$ and bending-mode force $\boldsymbol{F}_{B1}$; (**b**) Bending mode $\boldsymbol{B}_3$ and bending-mode force $\boldsymbol{F}_{B3}$; (**c**) Bending mode $\boldsymbol{B}_5$ and bending-mode force $\boldsymbol{F}_{B5}$; (**d**) Bending mode $\boldsymbol{B}_7$ and bending-mode force $\boldsymbol{F}_{B7}$; (**e**) Bending mode $\boldsymbol{B}_9$ and bending-mode force $\boldsymbol{F}_{B9}$; (**f**) Bending mode $\boldsymbol{B}_{11}$ and bending-mode force $\boldsymbol{F}_{B11}$; (**g**) Bending mode $\boldsymbol{B}_{13}$ and bending-mode force $\boldsymbol{F}_{B13}$; (**h**) Bending mode $\boldsymbol{B}_{15}$ and bending-mode force $\boldsymbol{F}_{B15}$; (**i**) Bending mode $\boldsymbol{B}_{17}$ and bending-mode force $\boldsymbol{F}_{B17}$; (**j**) Bending mode $\boldsymbol{B}_{19}$ and bending-mode force $\boldsymbol{F}_{B19}$.

Figure 5 shows that the higher the order, the higher the spatial frequency of the bending mode. In addition, some bending modes exhibited similarities with specific Zernike modes. For example, the first-order bending mode was similar to the astigmatism in the Zernike mode. The third-order bending mode was similar to the trefoil aberration. The fifth-order surface was similar to the defocus, and the seventh-order surface was similar to the quadrafoil aberration. Figure 6 shows a schematic of the amplitude of the bending-mode force. The figure shows that as the order i of the bending mode increased, the amplitude of the bending-mode force generally increased. Figures 5 and 6 validate the viewpoint proposed in Section 3.1.1, that the stiffness and frequency of $\boldsymbol{B}_i$ gradually increased with increasing order. This indicated that the bending-mode method could eliminate high-frequency components in the surface error and reduce the amplitude of the correction force.

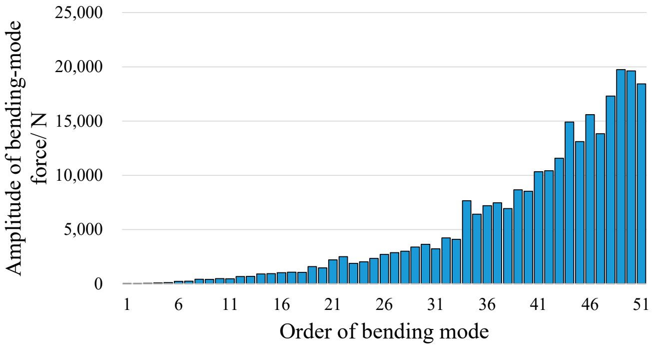

Figure 6. Relationship between the amplitude of bending-mode force $\boldsymbol{F}_{Bi}$ and the order i of the bending mode.

3.2. Pose Correction of the 4m SiC Primary Mirror

The six-hardpoint positioning mechanism consisted of six hardpoints of the same structure, which can be understood as linear displacement actuators with a high axial stiffness. When the length of the hardpoints remained unchanged, the rigid displacement of the primary mirror was limited, and the pose of the primary mirror remained unchanged. The pose of the primary mirror could be controlled by controlling the length of the hardpoints, thereby actively adjusting the pose of the primary mirror.

The structural diagram of the six-hardpoint positioning mechanism is shown in Figure 7, where Figure 7a shows the initial pose state of the mechanism and Figure 7b shows the state of the mechanism after a pose adjustment [29]. When considered as a rigid body, the primary mirror had six degrees of freedom, with $\boldsymbol{q} = [x\ y\ z\ \alpha\ \beta\ \gamma]^{\mathrm{T}}$ representing the pose of the primary mirror, where $\boldsymbol{q}$ could be decomposed into a position vector $\boldsymbol{t} = [x\ y\ z]^{\mathrm{T}}$ and attitude vector $\boldsymbol{s} = [\alpha\ \beta\ \gamma]^{\mathrm{T}}$. The relationship between the pose of the primary mirror and the length of the hardpoints was

$$\boldsymbol{l}_j = \boldsymbol{t} + \boldsymbol{R}\boldsymbol{a}_j - \boldsymbol{b}_j \tag{12}$$

where $j = 1, 2, \ldots, 6$ corresponds to the six hardpoints. $\boldsymbol{l}_i$ is the vector that represents the direction of the hardpoint, and the norm of the vector was the length of the hardpoint. $\boldsymbol{t}$ is the coordinate of origin O_1 of the coordinate system O_1-$\mathrm{x}_1\mathrm{y}_1\mathrm{z}_1$ in the coordinate system O-xyz. $\boldsymbol{a}_j$ is the coordinate of the upper support point A_j in the coordinate system O_1-$\mathrm{x}_1\mathrm{y}_1\mathrm{z}_1$, and $\boldsymbol{b}_j$ is the coordinate of the lower support point B_j in the coordinate system O-xyz. $\boldsymbol{R}$ is the rotation matrix:

$$\boldsymbol{R} = \begin{bmatrix} \cos\gamma\cos\beta & \cos\gamma\sin\beta\sin\alpha - \sin\gamma\cos\alpha & \cos\gamma\sin\beta\cos\alpha + \sin\gamma\sin\alpha \\ \sin\gamma\cos\beta & \sin\gamma\sin\beta\sin\alpha + \cos\gamma\cos\alpha & \sin\gamma\sin\beta\cos\alpha - \cos\gamma\sin\alpha \\ -\sin\beta & \cos\beta\sin\alpha & \cos\beta\cos\alpha \end{bmatrix} \tag{13}$$

where α, β, and γ are the rotation angles of the primary mirror around the coordinate taxes x_2, y_2, and z_2, respectively, and are the components of the attitude vector $\boldsymbol{s} = [\alpha\ \beta\ \gamma]^T$. Equation (12) is called the inverse kinematics model of the six-hardpoint positioning mechanism, and it established the relationship between the pose of the primary mirror and the length and direction of the hardpoints.

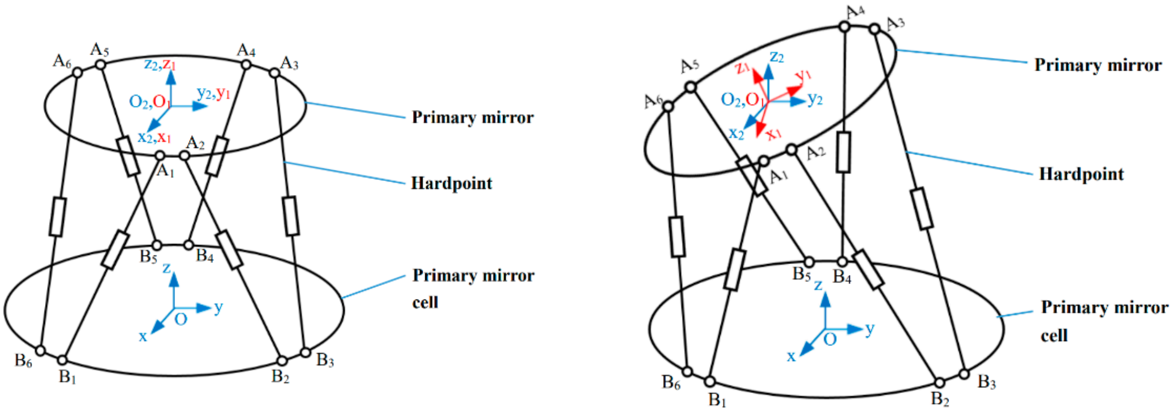

(**a**) (**b**)

Figure 7. Structural diagram of the six-hardpoint positioning mechanism. (**a**) Mechanism in the initial pose; (**b**) mechanism in the state after pose adjustment.

Based on the above theory, we could use the six-hardpoint positioning mechanism to compensate for and correct the primary mirror pose error caused by the mirror cell deformation. During a telescope observation, the mirror cell undergoes deformation due to its own gravity and the reaction force of the pneumatic actuators, which can lead to an error in the pose of the primary mirror. By changing the length of the hardpoints, the pose of the primary mirror can be corrected.

Considering the case of elevation angles of 45° and 90° as examples, the corresponding deformation of the mirror cell is shown in Figure 8. The deformation of the mirror cell caused a displacement at the lower support point of the hardpoint, as shown in Table 1. The displacement of the lower support point resulted in an error in the pose of the primary mirror. The pose errors of the primary mirror at different elevation angles were calculated, as shown in Figure 9.

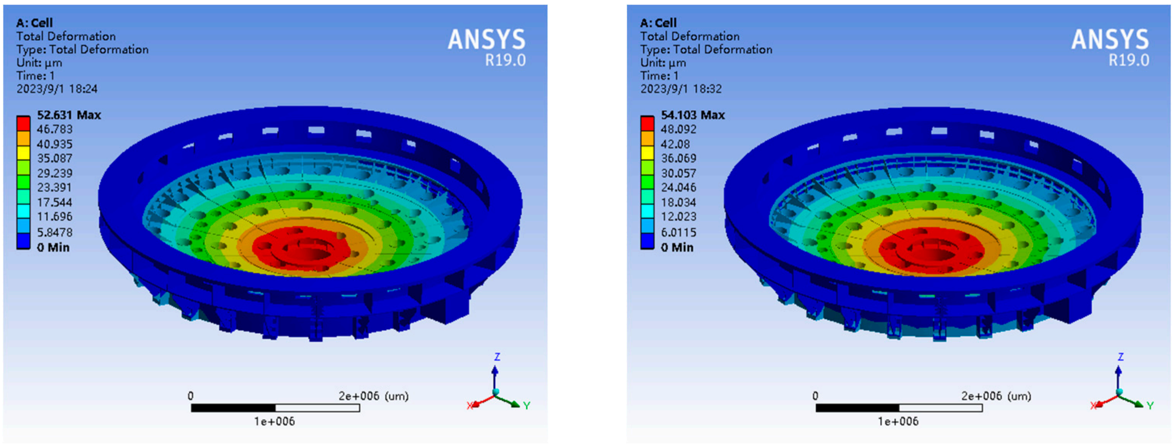

(**a**) (**b**)

Figure 8. Deformation diagram of the mirror cell. (**a**) Elevation angle of 45°; (**b**) Elevation angle of 90°.

Table 1. Displacement at the fixed point between the hardpoint and mirror cell.

Number of Hardpoints	Elevation Angle of 45°			Elevation Angle of 90°		
	dx/µm	dy/µm	dz/µm	dx/µm	dy/µm	dz/µm
1	−6.37	0.96	−13.77	−1.86	1.41	−19.54
2	−6.36	−1.04	−13.74	−1.61	−0.39	−18.92
3	−5.00	−1.72	−17.00	−0.67	−1.06	−19.79
4	−3.96	−0.30	−22.35	0.88	−0.05	−19.66
5	−3.97	0.23	−22.53	0.87	1.01	−19.55
6	−5.01	1.63	−17.13	−0.77	2.17	−19.86

Figure 9. Relationship between the pose error of the primary mirror and elevation angle.

The designed primary mirror support system corrected the pose of the primary mirror by adjusting the length of the hardpoints. The required amount of the adjustment could be calculated using Equation (12); the calculated results are shown in Figure 10. Owing to the symmetry of the spatial arrangement of the six hardpoints, the adjustment amounts of the two symmetrical hardpoints were similar. In addition, as the elevation angle increased, the adjustment amounts of all the hardpoints tended to be similar. When the elevation angle was 90°, the adjustment amounts of all the hardpoints were almost similar, because when the optical axis pointed towards the zenith, the primary mirror only had a position error in the direction of the optical axis, and there was no attitude error.

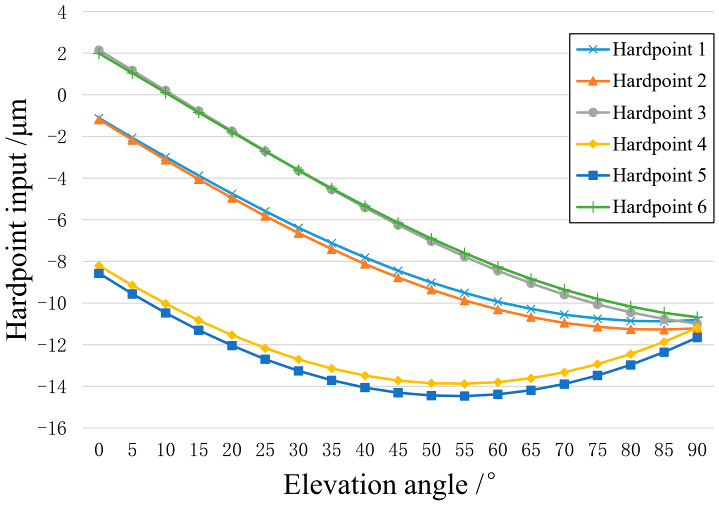

Figure 10. Adjustment amount of hardpoint length required to correct the primary mirror pose error.

3.3. Influence of Force on Hardpoints on the Surface Shape of the 4m SiC Primary Mirror and Compensation Methods

In the designed active support system, the pneumatic surface control actuators were not only used to correct the surface shape, but also to support the weight of the primary mirror. The above scheme was to avoid force being applied on the hardpoints, thereby improving surface accuracy. However, we found that the hardpoints were still subjected to a force for other reasons, resulting in a decrease in the surface shape accuracy of the primary mirror. We evaluated the reasons for the force on the hardpoints and proposed a method to solve this problem. The force of the hardpoints caused obvious protrusions and dents to remain in the corrected surface shape, as shown in Figure 11. These surface defects were high-frequency errors in space, which are difficult to correct with active optics.

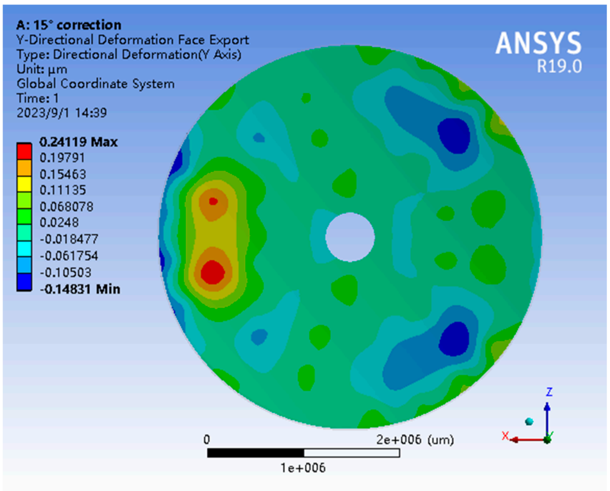

Figure 11. Primary mirror surface defects caused by force on hardpoints (external conditions: gravity; elevation angle: 15°; order of the bending modes: 40; the rms after surface correction: 53.9 nm).

The reasons for the force on the hardpoints were multifaceted. First, the pneumatic actuators provided an axial force to balance the axial component of the primary mirror gravity, while the two-axis actuators provided a radial force to balance the radial component. The magnitude of the resultant force $\boldsymbol{F}_G$ of the axial and radial forces was the same as the gravity $\boldsymbol{G}_{PM}$ of the primary mirror, whereas the direction was opposite. However, $\boldsymbol{F}_G$ and $\boldsymbol{G}_{PM}$ may not be collinear, resulting in the primary mirror being subjected to a moment, which, in turn, led to a force being exerted on the hardpoints. In addition, the primary mirror and entire system were subjected to thermal loads, wind loads, and inertial forces, which could also induce a force on the hardpoints. Due to the severe surface defects caused by the force on the hardpoints, compensation had to be provided for the force.

Our approach used pneumatic actuators to output a certain force onto the primary mirror to compensate for the force on the hardpoints before correcting the surface shape. The stationary primary mirror was in a state of force equilibrium, and the resultant force and moment of the primary mirror were 0. The resultant force and moment of the hardpoints on the primary mirror were calculated based on the force on each hardpoint. Subsequently, by applying the same force and moment to the primary mirror through the pneumatic actuators, the primary mirror could still be in a state of force equilibrium, but the force on the hardpoints was offset. This could eliminate the influence of the force on the hardpoints on the surface shape and compensate for the force exerted on the hardpoints.

First, the resultant force of the hardpoints on the primary mirror was calculated. Let the force on the hardpoint be F_{Dj}, with a positive value for compression and a negative value for tension, where $j = 1, 2, \ldots, 6$. Projecting the force on the hardpoints toward the coordinate axis gave

$$F_{DXj} = F_{Dj} \cos \alpha_D \tag{14}$$

$$F_{DYj} = F_{Dj} \cos \beta_D \tag{15}$$

$$F_{DZj} = F_{Dj} \cos \gamma_D \tag{16}$$

where F_{DXj}, F_{DYj}, and F_{DZj} are the projections of F_{Dj} along the x-, y-, and z-axes, respectively. α_D, β_D, and γ_D are the angles between F_{Dj} and the positive directions of the x-, y-, and z-axes, respectively. F_{DXj}, F_{DYj}, and F_{DZj} were summed to obtain the three components of the resultant force of the hardpoints on the primary mirror:

$$F_X = \sum_{j=1}^{6} F_{DXj} \tag{17}$$

$$F_Y = \sum_{j=1}^{6} F_{DYj} \tag{18}$$

$$F_Z = \sum_{j=1}^{6} F_{DZj} \tag{19}$$

Then, the three components of the resultant moment of the hardpoints on the primary mirror could be calculated as

$$M_X = \sum_{j=1}^{6} F_{DZj} y_j \tag{20}$$

$$M_Y = -\sum_{j=1}^{6} F_{DYj} x_j \tag{21}$$

$$M_Z = -\sum_{j=1}^{6} F_{DXj} y_j + \sum_{j=1}^{6} F_{DYj} x_j \tag{22}$$

where x_j and y_j are the x and y coordinates of the upper support point of the j-th hardpoint, respectively. To compensate for the force on the hardpoints, we used the pneumatic actuators to apply a force and moment equal to the resultant force and moment of the hardpoints to the primary mirror. That is, the resultant force and moment of the hardpoints were distributed over the pneumatic actuators.

Considering the installation direction of the two-axis pneumatic actuator, a specific actuator could only be used to output a force in a specific direction. The force F_X in the x-direction was distributed over actuators 1–18, 20–23, and 26–29. The output force $\boldsymbol{F}_{FX}$ of each actuator was $F_X/26$. The force F_Y in the y-direction was distributed over actuators 19, 24, 25, and 30. The output force $\boldsymbol{F}_{FY}$ was $F_Y/4$. The force F_Z in the z-direction was distributed over actuators 1–30, and the output force $\boldsymbol{F}_{FZ}$ was $F_Z/30$.

In terms of the moment distribution, the moments M_X and M_Y were generated by the z-direction force output by actuators 1–30. To generate M_X, the required output force for each actuator was

$$\boldsymbol{F}_{MXi} = M_X \boldsymbol{Y}_M / \sum_{i=1}^{30} |y_i| \tag{23}$$

where

$$\boldsymbol{Y}_M = \begin{bmatrix} y_1/|y_1| & y_2/|y_2| & \cdots & y_{30}/|y_{30}| \end{bmatrix}^T \tag{24}$$

where y_i is the y-direction coordinate of support point i. To generate M_Y, the output force required for the actuator was

$$\boldsymbol{F}_{MYi} = -M_Y \boldsymbol{X}_M / \sum_{i=1}^{30} |x_i| \tag{25}$$

where

$$\boldsymbol{X}_M = \left[x_1/|x_1| \quad x_2/|x_2| \quad \cdots \quad x_{30}/|x_{30}|\right]^T \tag{26}$$

where x_i is the x-direction coordinate of support point i. The moment M_Z was parallel to the z-axis and was generated by the y-direction radial force output by actuators 19, 24, 25, and 30. The required output force was

$$\boldsymbol{F}_{MZi} = -M_Z\boldsymbol{Y}_Z/\sum|y_i| \quad (i = 19,\ 24,\ 25,\ 30) \tag{27}$$

where

$$\boldsymbol{Y}_Z = \left[y_{19}/|y_{19}| \quad y_{24}/|y_{24}| \quad y_{25}/|y_{25}| \quad y_{30}/|y_{30}|\right]^T \tag{28}$$

In summary, to compensate for the force on the hardpoints, the combined force and moment of the hardpoints on the primary mirror were calculated. Then, the equivalent forces and moments were output through the pneumatic actuators to compensate for the force on the hardpoints. The forces output by the pneumatic actuators are listed in Table 2.

Table 2. Output force required for the pneumatic surface control actuators to compensate for the force on the hardpoints.

Force	Direction of Force	Role of Force	Number of the Actuator *i*	Value of Force/N
$\boldsymbol{F}_{\mathrm{FZi}}$	z	Compensate for F_Z	1–30	$F_Z/30$
$\boldsymbol{F}_{\mathrm{FXi}}$	x	Compensate for F_X	1–18, 20–23, 26–29	$F_X/26$
$\boldsymbol{F}_{\mathrm{FYi}}$	y	Compensate for F_Y	19, 24, 25, 30	$F_Y/4$
$\boldsymbol{F}_{\mathrm{MXi}}$	z	Compensate for M_X	1–30	$M_X\boldsymbol{Y}_M/\sum_{i=1}^{30}\|y_i\|$
$\boldsymbol{F}_{\mathrm{MYi}}$	z	Compensate for M_Y	1–30	$-M_Y\boldsymbol{X}_M/\sum_{i=1}^{30}\|x_i\|$
$\boldsymbol{F}_{\mathrm{MZi}}$	y	Compensate for M_Z	19, 24, 25, 30	$-M_Z\boldsymbol{Y}_Z/\sum\|y_i\|$

4. Performance Evaluation of the Active Support System for the 4m SiC Primary Mirror

4.1. Verification of the Bending Mode

In Section 3.1.2, the theoretical values of 51 orders of valid bending modes of the 4m SiC primary mirror were obtained. To compare the theoretical and actual values of the bending modes, the bending mode forces $\boldsymbol{F}_{Bi}$ were sequentially applied to the primary mirror, and the responses of $\boldsymbol{F}_{Bi}$ were the actual values of the bending mode $\boldsymbol{B}_i$. The results are shown in Figure 12. Figures 5 and 12 show that the theoretical and actual values of most $\boldsymbol{B}_i$ values were very similar. However, certain differences existed between the theoretical and actual values of the first- and seventh-order bending modes. This was because the tilt was eliminated in Figure 5, but not in Figure 12. Overall, the designed support system for the 4m SiC primary mirror could accurately generate various bending modes.

4.2. Correction of Gravity Deformation of the Primary Mirror

Under the action of gravity, the primary mirror underwent a deformation related to the elevation angle, which refers to the angle between the optical axis of the telescope and the horizontal direction. When studying the gravity deformation, we focused on the situations where the elevation angles were 90°, 45°, and 0°. The gravity deformations under the three elevation angle conditions are shown in Figure 13.

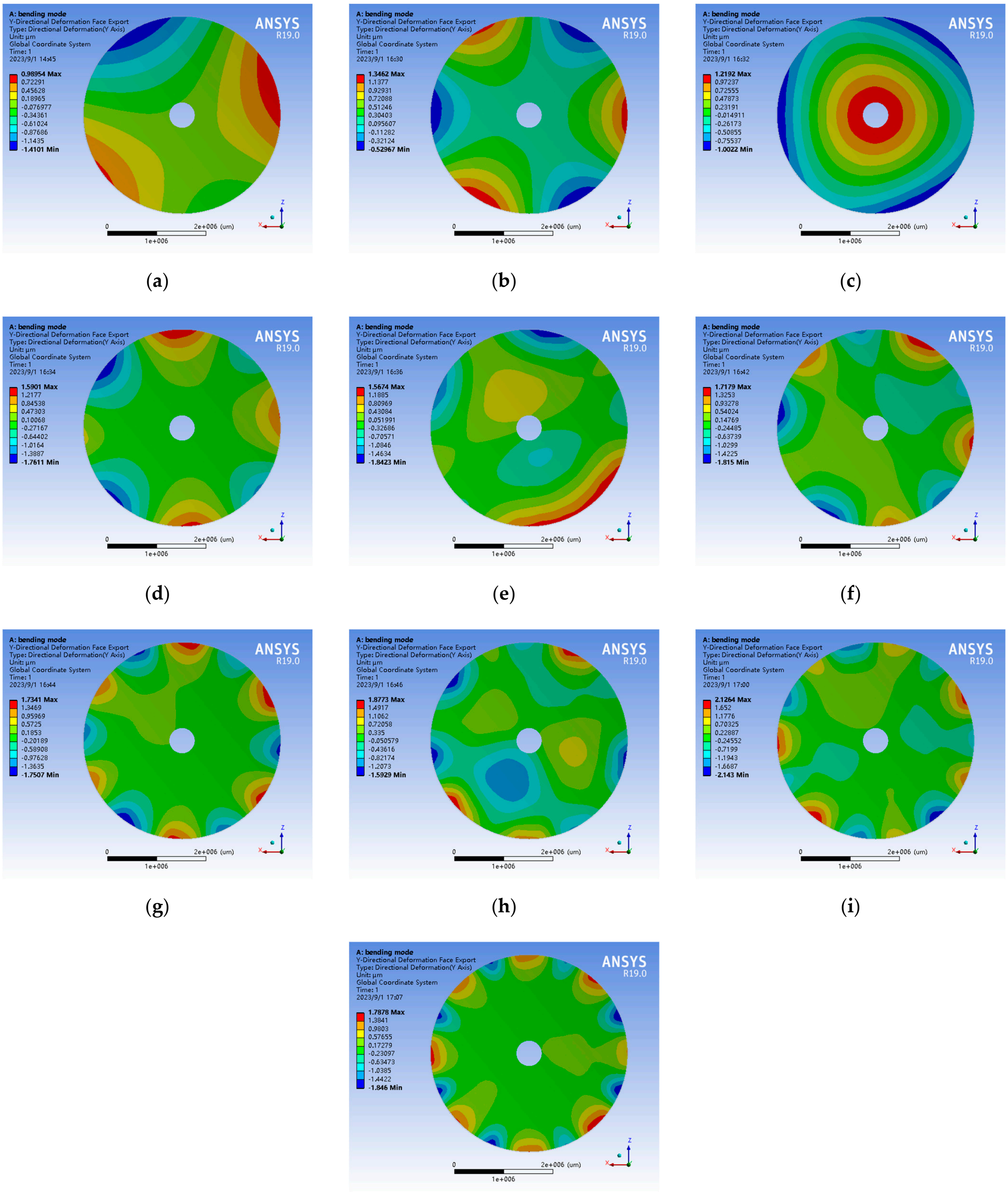

Figure 12. Actual values of partial bending mode B_i of the 4m SiC primary mirror. (**a**) Actual values of B_1; (**b**) Actual values of B_3; (**c**) Actual values of B_5; (**d**) Actual values of B_7; (**e**) Actual values of B_9; (**f**) Actual values of B_{11}; (**g**) Actual values of B_{13}; (**h**) Actual values of B_{15}; (**i**) Actual values of B_{17}; (**j**) Actual values of B_{19}.

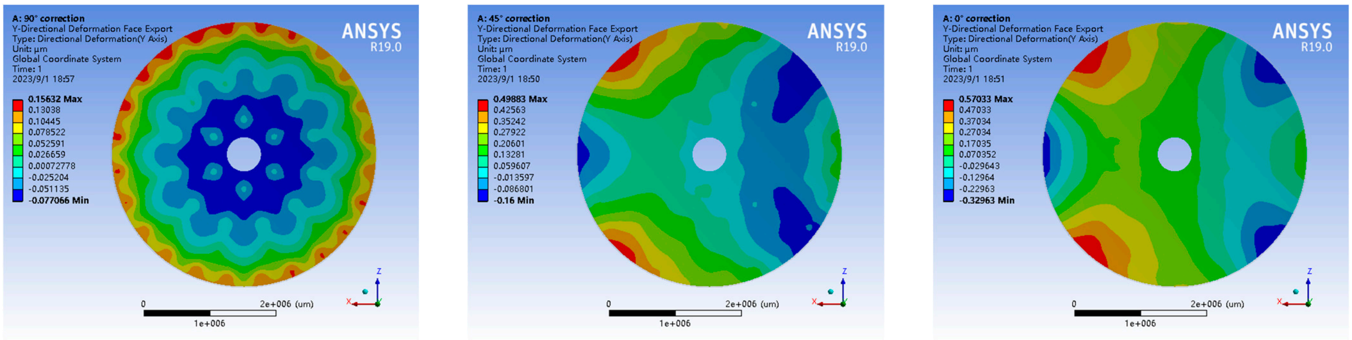

(**a**) (**b**) (**c**)

Figure 13. Schematic diagram of the deformation of the 4m SiC primary mirror surface due to gravity. (**a**) Elevation angle of 90°; (**b**) Elevation angle of 45°; (**c**) Elevation angle of 0°.

To verify the proposed compensation method for the force on the hardpoints, we attempted to use the first 40 orders of bending modes to correct the gravity deformation of the primary mirror at an elevation angle of 45°. The surface shape before the correction is shown in Figure 13b, with a rms of 165.3 nm. If the force on the hardpoint was not compensated, the corrected result was as shown in Figure 14a. At the position where the hardpoints came into contact with the back plate of the primary mirror, the surface of the mirror showed obvious protrusions and dents. The rms of the surface shape was 50.4 nm. From both the data and image perspectives, the surface shape was very poor. Based on Figure 13b, we compensated for the force on the hardpoints and obtained the situation shown in Figure 14b, which had a surface shape rms of 129.1 nm. After the force was compensated for, the surface correction was performed again, and the first 40 orders of bending modes were also used. The results are shown in Figure 14c. The rms of the surface shape in Figure 14c was 12.4 nm, which was less than the $\lambda/30$ (λ = 632.8 nm) requirement. A comparison of Figure 14a,c showed that compensating for the force on the hardpoints played an important role in improving the accuracy of the corrected primary mirror surface shape, with the rms of the surface shape reduced from 50.4 nm to 12.4 nm. This result also preliminarily proved the effectiveness of the surface shape correction based on the bending modes.

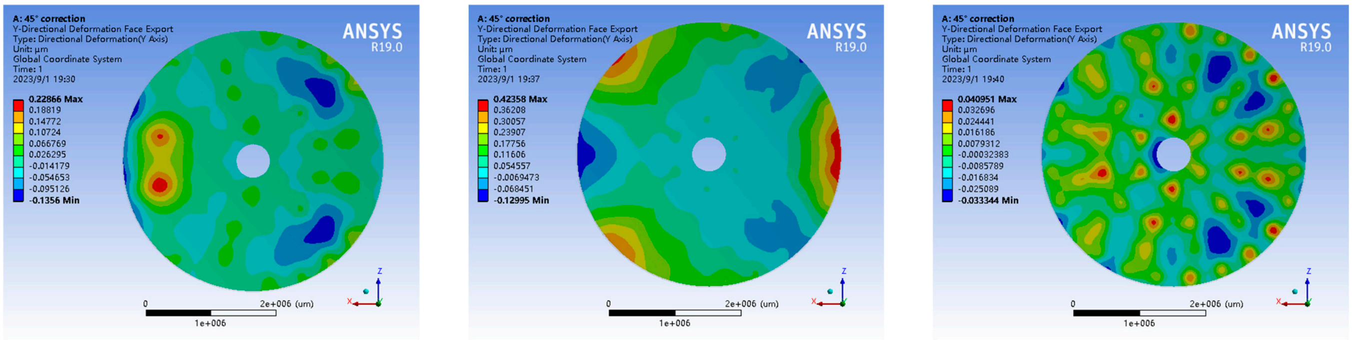

(**a**) (**b**) (**c**)

Figure 14. Correction of gravity deformation of the primary mirror using the first 40 orders of bending modes at an elevation angle of 45°. (**a**) Surface shape correction result (force on hardpoint not compensated); (**b**) Surface shape before correction (force on hardpoint compensated); (**c**) Surface shape correction result (force on hardpoint compensated).

4.3. Relationship between the Orders of Bending Modes and the Correction Effect

For the 4m SiC primary mirror and the designed support system, there were 51 available bending modes. If only the first few orders of the bending modes were used to calculate the correction force, the amplitude of the force could be reduced. To ensure a good accuracy was attained for the corrected primary mirror shape, the order of the bending modes used in the correction had to be determined. Therefore, we conducted a series of simulations at elevation angles of 90°, 45°, and 0°, and the gravity deformation of the primary mirror was corrected using different orders of bending modes. The corrected primary mirror shape and the amplitude of the correction force are shown in Figure 15, where the horizontal axis represents the order of the bending modes used for the surface correction, the vertical axis on the left represents the rms of the corrected primary mirror shape, and the vertical axis on the right represents the amplitude of the correction force. Figure 15 shows that as the orders of the bending modes used increased, the rms of the primary mirror shape gradually decreased, and the amplitude of the correction force gradually increased. Therefore, if too many orders of bending modes was used, the amplitude of the correction force could not be reduced. If too few orders were used, the corrected surface shape accuracy would be poor. After comprehensive considerations, we believe that using the first 30 orders of bending modes for the surface shape correction was the most reasonable. This not only effectively reduced the amplitude of the correction force, but also ensured a good accuracy was achieved for the corrected primary mirror surface shape.

The corrected surface shapes using the first 30 orders of bending modes are shown in Figure 16, and the relevant data before and after the surface shape correction are listed in Table 3. A comparison of Figures 13 and 16 revealed that the corrected primary mirror surface was significantly improved. According to Table 3, the rms values of the corrected surface shape under the three elevation angles were less than 16 nm, which met the requirement of being less than $\lambda/30$ (λ = 632.8 nm). The above results indicated that using the first 30 orders of bending modes was sufficient to effectively correct the gravity deformation of a 4m SiC primary mirror.

Table 3. Relevant data of the primary mirror surface shape before and after correction for gravity deformation.

Elevation Angle	**Primary Mirror Surface Shape rms/nm**		**Amplitude of the Correction Force/N**	**Maximum Von Mises Stress of the Primary Mirror/MPa**
	Before Calibration	**After Correction**		
90°	64.8	14.8	51.3	0.51
45°	165.3	14.5	59.6	0.96
0°	211.0	15.8	57.2	1.18

The Zernike polynomial was used to fit the surface shape before and after the correction, as shown in Figure 17. Due to space limitations, only the results at the elevation angle of 90° were given. The main components of the surface shape error before the correction were defocus and spherical aberration. The corrected surface shape significantly improved.

4.4. Correction of the Primary Mirror Surface Shape Errors Caused by Thermal and Wind Loads

In addition to gravity, thermal and wind loads could deform the primary mirror, thereby affecting its surface accuracy and the imaging quality of the telescope. This section analyzes the effects of the thermal and wind loads, and corrects the corresponding surface shape errors.

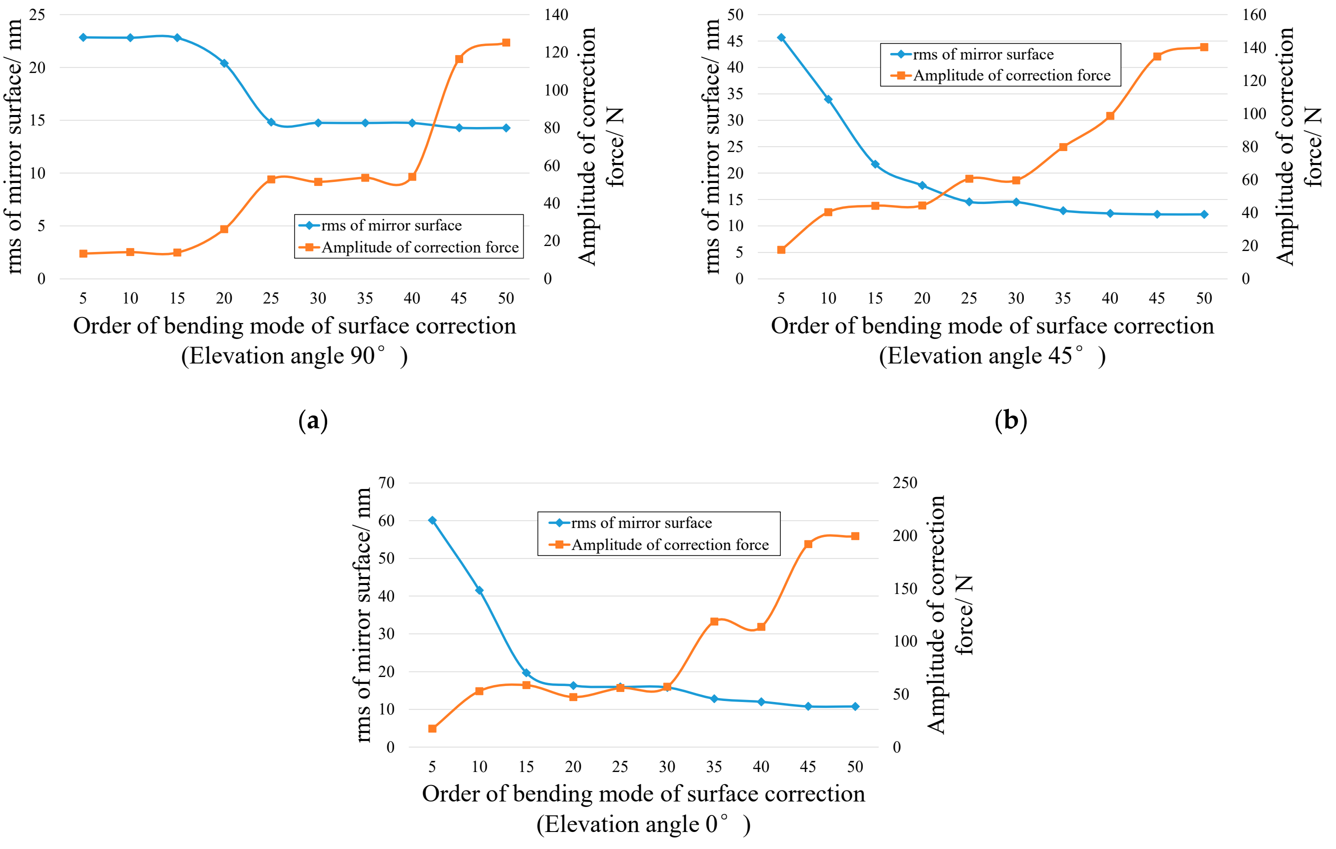

(**a**) (**b**)

(**c**)

Figure 15. Results of correcting gravity deformation of the primary mirror using different orders of bending modes. (**a**) Results at elevation angle of 90°; (**b**) Results at elevation angle of 45°; (**c**) Results at elevation angle of 0°.

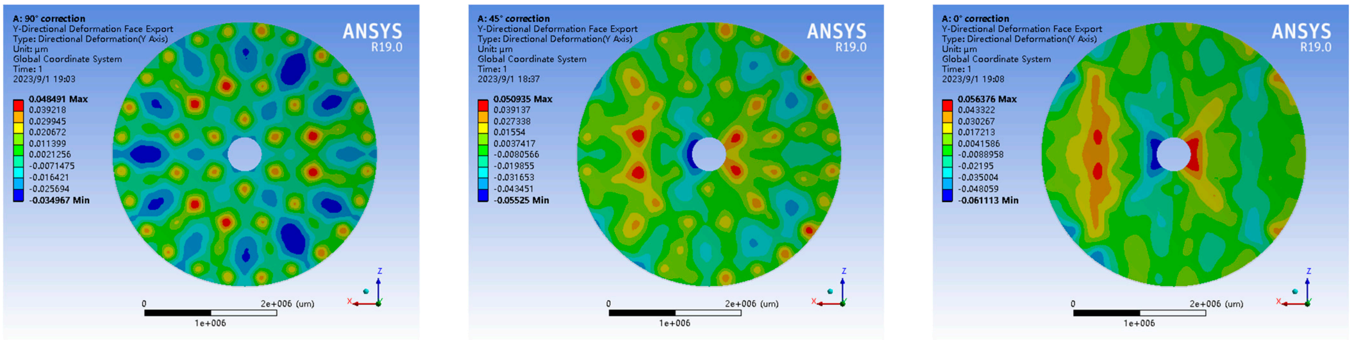

(**a**) (**b**) (**c**)

Figure 16. Results of correcting the gravity deformation of the primary mirror using the first 30 orders of bending modes. (**a**) Elevation angle of 90°; (**b**) Elevation angle of 45°; (**c**) Elevation angle of 0°.

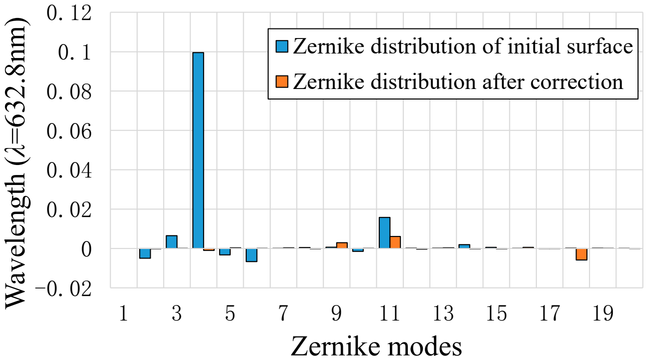

Figure 17. Zernike distributions of surface before and after correction (elevation angle of 90°).

4.4.1. Thermal Load

SiC has a high specific stiffness and good thermal stability, making it an ideal mirror material. The main indexes of RB SiC (reaction-bonded silicon carbide) are as follows: density 3050 $\mathrm{kg/m^3}$, Young's modulus 392,000 MPa, Poisson's ratio 0.25, thermal expansion coefficient $2.5 \times 10^{-6}/\mathrm{K}$, and thermal conductivity 185 $\mathrm{W/(m{\cdot}K)}$ [30]. Due to SiC having a large thermal expansion coefficient, a primary mirror composed of SiC is sensitive to changes in the environment's temperature, and analyzing this thermal deformation is necessary [31,32]. The designed active support system could actively correct the thermal deformation of the 4m SiC primary mirror to reduce the deformation of the mirror surface and improve the imaging quality of the telescope.

Regarding the thermal load of the 4m SiC primary mirror, three representative temperature cases were considered: the axial, radial, and transverse temperature differences of the primary mirror. Figure 18 shows the temperature fields in the three situations for a temperature difference of 0.2 °C. The three temperature fields were applied to a 4m SiC primary mirror; the deformation of the mirror surface is shown in Figure 19.

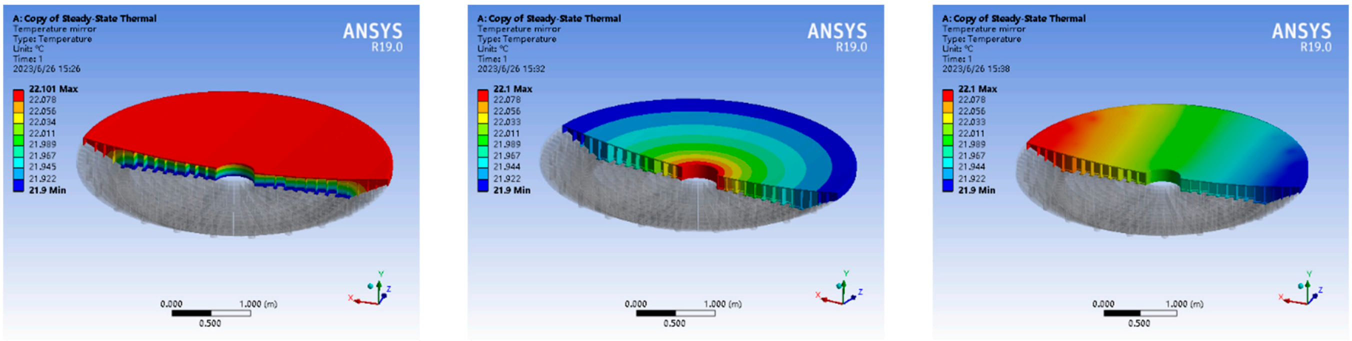

(**a**) (**b**) (**c**)

Figure 18. Three temperature fields corresponding to three types of temperature differences. (**a**) Temperature field of 0.2 °C axial temperature difference; (**b**) Temperature field of 0.2 °C radial temperature difference; (**c**) Temperature field of 0.2 °C transverse temperature difference.

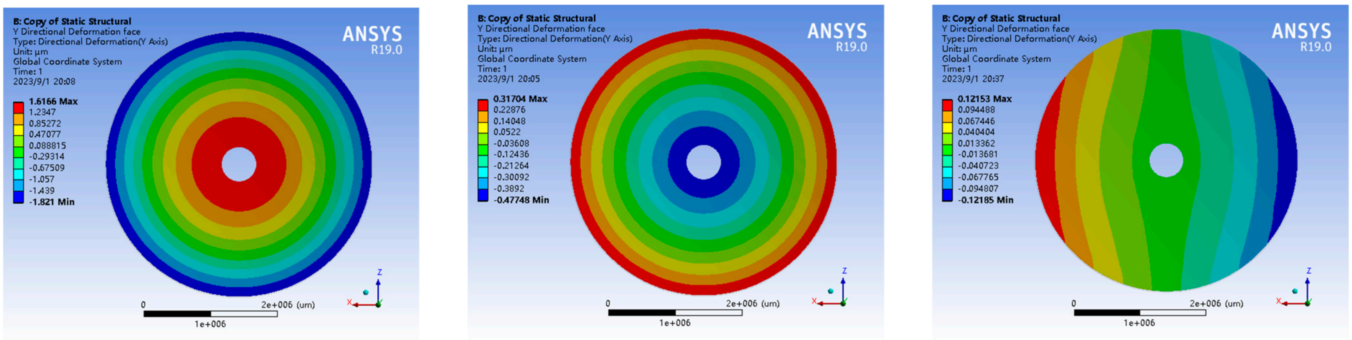

(**a**) (**b**) (**c**)

Figure 19. The 4m SiC primary mirror surface shape caused by three types of temperature differences. (**a**) Axial temperature difference of 0.2 °C; (**b**) Radial temperature difference of 0.2 °C; (**c**) Transverse temperature difference of 0.2 °C.

The first 30 orders of bending modes were used to perform an active optics correction on the above surface shape, and the results are shown in Figure 20. The rms values of the primary mirror surface shape before and after the correction are listed in Table 4. Under the axial temperature difference of 0.2 °C, the rms decreased from 1026.7 to 14.9 nm, indicating a significant correction effect. The rms of the other two cases also decreased significantly after the correction. The designed support system had a good correction effect on the thermal deformation of the primary mirror.

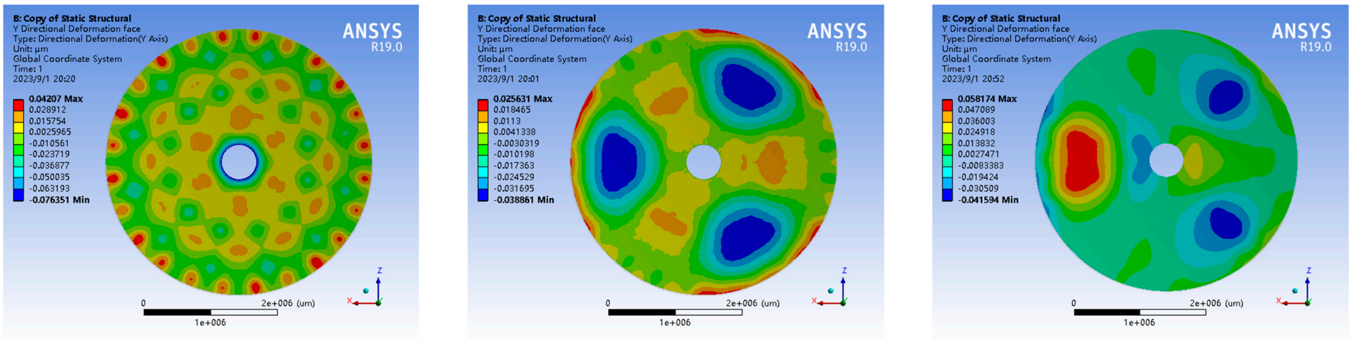

(**a**) (**b**) (**c**)

Figure 20. Results of correcting the thermal load deformation of the primary mirror using the first 30 orders of bending modes. (**a**) Axial temperature difference of 0.2 °C; (**b**) Radial temperature difference of 0.2 °C; (**c**) Transverse temperature difference of 0.2 °C.

Table 4. Relevant data of the primary mirror surface shape before and after correction for thermal load deformation.

Temperature Field	Primary Mirror Surface Shape rms/nm		Amplitude of the Correction Force/N	Maximum Von Mises Stress of the Primary Mirror/MPa
	Before Calibration	After Correction		
Axial temperature difference of 0.2 °C	1026.7	14.9	303.8	0.34
Radial temperature difference of 0.2 °C	196.2	16.4	60.7	0.15
Transverse temperature difference of 0.2 °C	58.7	17.7	125.3	0.15

The Zernike polynomial was used to fit the surface shape (axial temperature difference of 0.2 °C) before and after the correction, as shown in Figure 21. The surface correction eliminated the defocus and spherical aberration.

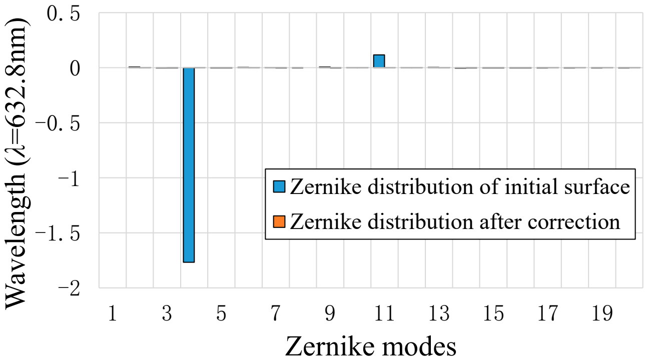

Figure 21. Zernike distributions of surface before and after correction (axial temperature difference of 0.2 °C).

In addition, we performed surface corrections for the other temperature differences. The first 30 orders of bending modes were again used, and the results are shown in Figure 22. Setting the rms to $<\lambda/30$ (λ = 632.8 nm) as the standard, the results indicated that the designed active support system could effectively correct the 4m SiC primary mirror surface shape error caused by an axial temperature difference of 0.25 °C, radial temperature difference of 0.25 °C, and transverse temperature difference of 0.2 °C.

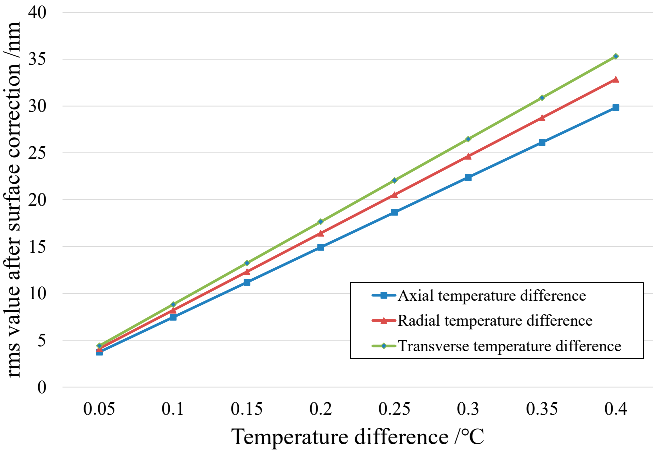

Figure 22. Results of correcting the thermal load deformation of 4m SiC primary mirror with the first 30 orders of bending modes.

4.4.2. Wind Load

The primary mirrors of modern large telescopes are often directly exposed to air during operation, resulting in a wind load deformation. The wind load exerted on the primary mirror can be divided into two parts: static and dynamic wind load. The static wind load remains static or changes very slowly, whereas the dynamic wind load changes over time with a frequency that can reach several hertz [33].

Unlike adaptive optics, which corrects for atmospheric turbulence, active optics is used to correct the errors of the telescope itself. The correction object of active optics is the large-aperture primary mirror with a large mass, rather than the small-aperture deformable mirror used in adaptive optics. Therefore, the correction frequency of active optics is generally very low, which is clearly different from that of adaptive optics, whose correction frequency reaches several hundred hertz. Active optics is used to correct manufacturing errors in the primary mirror, surface errors caused by gravity and temperature, and surface errors caused by telescope movements. The frequency of these errors is below 1 Hz [34]. The calibration frequency of the designed active support system is 1 Hz; therefore, it could not correct the deformation caused by dynamic wind loads. In summary, only the influence and correction of a static wind load were analyzed.

The effect of the wind load is transmitted through wind pressure [35], which could be expressed as

$$P = \frac{1}{2}\rho v^2 \tag{29}$$

where P is the wind pressure, ρ is the air density, and v is the wind speed. The wind load force could be expressed as

$$F_W = PC_D A = \frac{1}{2}\rho v^2 C_D A \tag{30}$$

where F_W is the force exerted by the wind load on the structure, C_D is the wind-resistance coefficient, and A is the windward area of the structure.

An observation station at the National Astronomical Observatory of the Chinese Academy of Sciences was considered as an example. The altitude of the observation station is 900 m. According to the wind speed data from 2007 to 2014, the wind speed was mostly less than 15 m/s, with an average wind speed of approximately 2 m/s [36]. Therefore, in this analysis, the wind speed was set to 15 m/s. The density of air was 1.29 kg/m^3, and the wind pressure was calculated as 145.13 Pa, according to Equation (29).

In addition, according to Equation (30), the effect of the wind load calculation had to consider the windward area. The angle between the wind direction and the optical axis was set as θ, as shown in Figure 23. The windward area was inversely proportional to θ; θ was sequentially set to 0°, 30°, and 60°, and the tests were conducted. The surface shape of the 4m SiC primary mirror under the wind load is shown in Figure 24. The first 30 orders of bending modes were used to correct the surface shape, and the results are shown in Figure 25. The surface shape data before and after the correction are listed in Table 5. The rms of the corrected surface shape was less than 2 nm, indicating that the designed system could effectively correct the static wind load deformation of the primary mirror.

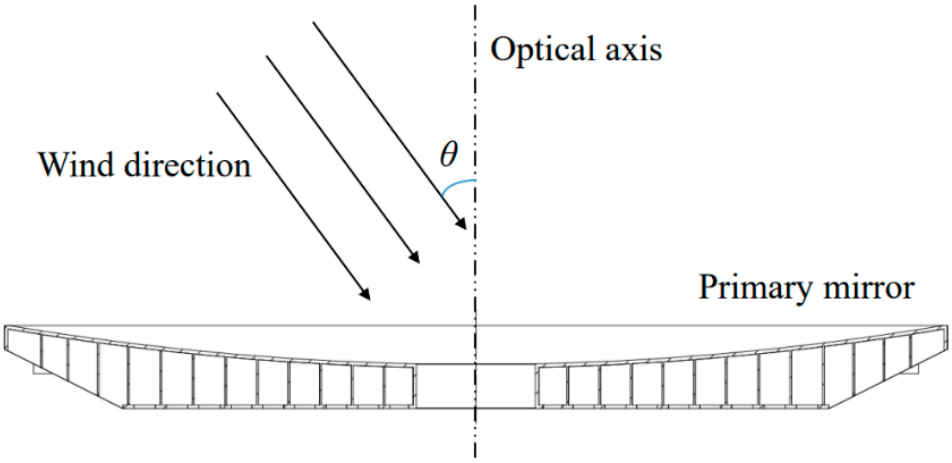

Figure 23. Schematic diagram of the 4m SiC primary mirror under wind load.

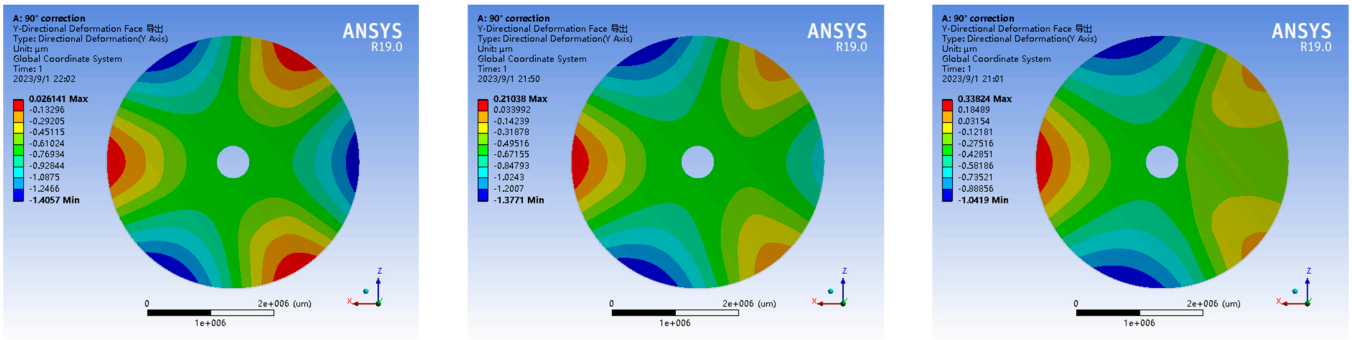

(**a**) (**b**) (**c**)

Figure 24. Schematic diagram of the deformation of the 4m SiC primary mirror surface due to static wind load. (**a**) θ = 0°; (**b**) θ = 30°; (**c**) θ = 60°.

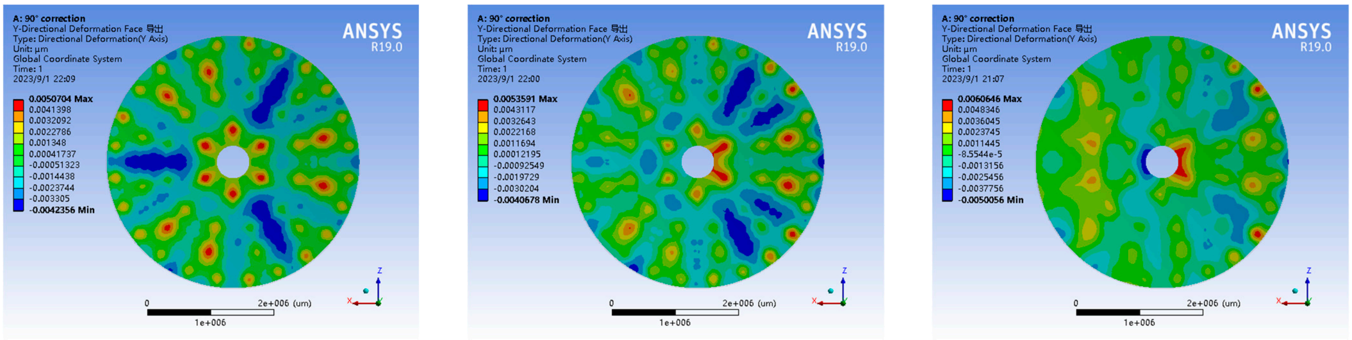

(**a**) (**b**) (**c**)

Figure 25. Correction results for the deformation of the primary mirror under static wind load using the first 30 orders of bending modes. (**a**) θ = 0°; (**b**) θ = 30°; (**c**) θ = 60°.

Table 5. Relevant data of the primary mirror surface shape before and after correction for static wind load deformation.

θ	Primary Mirror Surface Shape rms/nm		Amplitude of the Correction Force/N	Maximum Von Mises Stress of the Primary Mirror/MPa
	Before Calibration	After Correction		
0°	741.2	1.8	596.0	0.061
30°	656.3	1.6	631.3	0.092
60°	440.4	1.6	522.9	0.126

The Zernike polynomial was used to fit the surface shape (θ = 0°) before and after the correction, as shown in Figure 26. The surface correction eliminated the defocus, trefoil aberration, and spherical aberration.

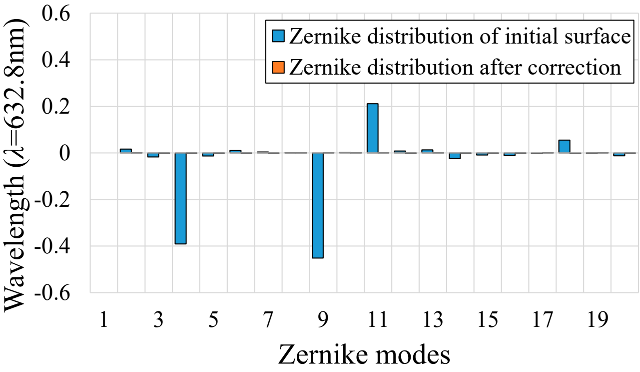

Figure 26. Zernike distributions of surface before and after correction (θ = 0°).

5. Conclusions

This study designed an active support system for a 4m SiC primary mirror, which could effectively reduce the surface error caused by various loads on the primary mirror and improve the imaging quality of the telescope. Firstly, the principle and structure of the designed system were explained. Then, a method for calculating the correction force through bending modes was derived, and the primary mirror pose correction based on the six-hardpoint positioning mechanism was verified. In response to the problem of protrusions and dents on the primary mirror surface caused by the force on the hardpoints, a method to compensate for the force on the hardpoints was proposed, reducing the rms of the corrected primary mirror surface from 50.4 nm to 12.4 nm. To achieve better results in the surface shape correction based on the bending modes, the relationship between the order of the bending modes used in the surface shape correction and the correction effect was studied. The results showed that using the first 30 orders of bending modes could effectively reduce the amplitude of the correction force and ensure a good surface shape accuracy. Finally, a performance evaluation was conducted on the designed system. We used the first 30 orders of bending modes to correct the deformation of the primary mirror under gravity, thermal load, and wind load. Under these three working conditions, the primary mirror surface error met the criterion of rms $<\lambda/30$ (λ = 632.8 nm) after the correction. In summary, the designed active support system could meet the surface shape accuracy index of the primary mirror. This study not only verified the application of active optics technology based on the eigenmode in large-aperture SiC mirrors, but also improved the relevant theoretical research of active optics and bending modes. The research has innovation and engineering significance.

There are two main aspects for future work planning. We plan to study the impact of dynamic wind loads on the primary mirror surface shape in a future work and to attempt to correct the low-frequency components. In addition, we also plan to conduct research on the thermal control system of the 4m SiC primary mirror.

Author Contributions: Conceptualization, Z.Y.; methodology, Z.Y. and X.W.; software, Z.Y.; validation, Z.Y., X.W. and F.W.; data curation, Z.Y.; writing—original draft preparation, Z.Y.; writing—review and editing, Z.Y., X.W. and F.W.; supervision, F.W.; funding acquisition, X.W. All authors have read and agreed to the published version of the manuscript.

Funding: This research was funded by the National Natural Science Foundation of China (no. 12133009).

Institutional Review Board Statement: Not applicable.

Informed Consent Statement: Not applicable.

Data Availability Statement: All data included in this study are available upon request through contact with the corresponding author.

Conflicts of Interest: The authors declare no conflict of interest.

References

1. Wilson, R.N.; Franza, F.; Noethe, L. Active Optics I. A System for Optimizing the Optical Quality and Reducing the Costs of Large Telescopes. *J. Mod. Opt.* **1987**, *4*, 485–509. [CrossRef]
2. Noethe, L.; Franza, F.; Giordano, P.; Wilson, R.N.; Citterio, O.; Conti, G.; Mattaini, E. Active Optics II. Results of an Experiment with a Thin 1 m Test Mirror. *J. Mod. Opt.* **1988**, *35*, 1427–1457. [CrossRef]
3. Wilson, R.N.; Franza, F.; Giordano, P.; Noethe, L.; Tarenghi, M. Active Optics III. Final Results with the 1 m Test Mirror and NTT 3·58 m Primary in the Workshop. *J. Mod. Opt.* **1989**, *36*, 1415–1425. [CrossRef]
4. Wilson, R.N.; Franza, F.; Noethe, L.; Andreoni, G. Active Optics IV. Set-up and Performance of the Optics of the ESO New Technology Telescope (NTT) in the Observatory. *J. Mod. Opt.* **1991**, *38*, 219–243. [CrossRef]
5. Xu, J.; Li, W.; Wang, K.; Hao, Q.; Lin, G. Design of a 2 m Primary Mirror Assembly Considering Fatigue Characteristics. *Appl. Sci.* **2022**, *12*, 10326. [CrossRef]
6. Muller, G.P.; Hileman, E.A.; Daruich, F.; Warner, M.; Wiecha, O.M.; Araujo, C.; Mills, N.G.; Johnson, B.E.; Stover, E.; Booth, M.T.; et al. LSST M1M3 figure actuator final design, fabrication, and test. *Proc. SPIE* **2018**, *11703*, 11703V. [CrossRef]
7. Tarenghi, M.; Wilson, R.N. The ESO NTT (New Technology Telescope): The First Active Optics Telescope. *Proc. SPIE* **1989**, *1114*, 302–313. [CrossRef]
8. Schipani, P.; Noethe, L.; Magrin, D.; Kuijken, K.; Arcidiacono, C.; Argomedo, J.; Capaccioli, M.; Dall'Ora, M.; D'Orsi, S.; Farinato, J.; et al. Active optics system of the VLT Survey Telescope. *Appl. Opt.* **2016**, *55*, 1573–1583. [CrossRef] [PubMed]
9. Minowa, Y.; Takato, N.; Iwata, I.; Hattori, T. An overview of current and future instrumentation at the Subaru telescope. *Proc. SPIE* **2016**, *9908*, 990806. [CrossRef]
10. Neufeld, C.; Zolcinski-Couet, M.C.; Keane, M.; Ruthven, G. The active primary mirror assembly for the SOAR telescope. *Proc. SPIE* **2004**, *5489*, 870–880. [CrossRef]
11. Vigil, M.L.; Witte, D.J.; LeVan, P.D.; Wallentine, P.J.; Briscoe, D.E.; Anderson, D.L. Sensor suite for the Advanced Electro-Optical System (AEOS) 3.6-m telescope. *Proc. SPIE* **1996**, *2819*, 151–169. [CrossRef]
12. Huedepohl, G.; Tamai, R.; Ehrenfeld, G.; Stranghellini, S.; Kraus, M. Integration and handling of the VLT primary and secondary mirror systems. *Proc. SPIE* **2000**, *4004*, 457–470. [CrossRef]
13. Huang, E. Gemini primary mirror cell design. *Proc. SPIE* **1997**, *2871*, 151–169. [CrossRef]
14. Williams, G.G.; Ortiz, R.; Goble, W.; Gibson, J.D. The 6.5-m MMT Telescope: Status and plans for the future. *Proc. SPIE* **2016**, *9906*, 99060V. [CrossRef]
15. Crass, J.; Bechter, A.; Sands, B.; King, D.L.; Ketterer, R.; Engstrom, M.; Hamper, X.; Kopon, D.; Smous, J.; Crepp, J.R.; et al. Final design and on-sky testing of the iLocater SX acquisition camera: Broad-band single-mode fibre coupling. *Mon. Not. R. Astron. Soc.* **2021**, *501*, 2250–2267. [CrossRef]
16. Meeks, R.L.; Ashby, D.; Biddick, C.; Devries, J.; Gusick, M.; Kern, J. Super hardpoints for the Large Binocular Telescope. *Proc. SPIE* **2010**, *7733*, 77335H. [CrossRef]
17. Neill, D.; Angeli, G.; Claver, C.; Hileman, E.; DeVries, J.; Sebag, J.; Xin, B. Overview of the LSST active optics system. *Proc. SPIE* **2014**, *9150*, 91500G. [CrossRef]
18. Yin, J.E.; Eisenstein, D.J.; Finkbeiner, D.P.; Stubbs, C.W.; Wang, Y. Active Optical Control with Machine Learning: A Proof of Concept for the Vera C. Rubin Observatory. *Astron. J.* **2021**, *161*, 216. [CrossRef]
19. Schipani, P.; D'Orsi, S.; Ferragina, L.; Fierro, D.; Marty, L.; Molfese, C.; Perrotta, F. Active optics primary mirror support system for the 2.6m VST telescope. *Appl. Opt.* **2010**, *49*, 1234–1241. [CrossRef]
20. Li, W.; Tang, J.; Guo, Y.; Rao, C. Active correction experiments on a 4-m thin primary mirror. *Opt. Express* **2021**, *29*, 41920–41931. [CrossRef]
21. Wang, H.; Zuo, Y.; Zheng, X.; Yang, J. Free-vibration modes of an annular mirror for the optical aberration representation. *J. Astron. Telesc. Instrum. Syst.* **2019**, *5*, 024002. [CrossRef]
22. Wang, H.; Liang, M.; Yao, D.; Zuo, Y.; Zheng, X.; Yang, J. Study on the application of the freevibration modes of an annular mirror in the active optics system. *J. Astron. Telesc. Instrum. Syst.* **2020**, *6*, 019002. [CrossRef]
23. Martin, H.M.; Davison, W.B.; DeRigne, S.T.; Hill, J.M.; Hille, B.B.; Meeks, R.L.; Trebisky, T.J. Active supports and force optimization for a 3.5-m honeycomb sandwich mirror. *Proc. SPIE* **1994**, *2119*, 251–262. [CrossRef]
24. Li, W.; Tang, J.; Guo, Y.; Rao, C. Constrained least-squares algorithm for active optics correction of a primary mirror. *Appl. Opt.* **2022**, *61*, 108–114. [CrossRef]
25. Martin, H.M.; Callahan, S.P.; Cuerden, B.; Davison, W.B.; DeRigne, S.T.; Dettmann, L.R.; Parodi, G.; Trebisky, T.J.; West, S.C.; Williams, J.T. Active supports and force optimization for the MMT primary mirror. *Proc. SPIE* **1998**, *3352*, 412–423. [CrossRef]
26. Martin, H.M.; Cuerden, B.; Dettmann, L.R.; Hill, J.M. Active optics and force optimization for the first 8.4-m LBT mirror. *Proc. SPIE* **2004**, *5489*, 826–837. [CrossRef]
27. Lan, B.; Wu, X.; Li, J.; Ming, M.; Liu, X.; Yang, H. Influence of axial-force errors on the deformation of the 4 m lightweight mirror and its correction. *Appl. Opt.* **2017**, *56*, 611–619. [CrossRef]
28. Yu, Z.; Wu, X.; Wang, F. Optimal design of parameters of the six-hardpoint positioning mechanism for large aperture primary mirror. *Opt. Precis. Eng.* **2023**, *31*, 200–213. [CrossRef]
29. Yu, Z.; Wu, X.; Wang, F. Kinematic Calibration Method for Six-Hardpoint Positioning Mechanisms Using Optimal Measurement Pose. *Appl. Sci.* **2023**, *13*, 4824. [CrossRef]

30. Qu, Y.; Jiang, Y.; Feng, L.; Li, X.; Liu, B.; Wang, W. Lightweight Design of Multi-Objective Topology for a Large-Aperture Space Mirror. *Appl. Sci.* **2018**, *8*, 2259. [CrossRef]
31. Greenhalgh, R.J.S.; Stepp, L.M.; Hansen, E.R. Gemini primary mirror thermal management system. *Proc. SPIE* **1994**, *2199*, 911–921. [CrossRef]
32. Hermann, K.G.; Finley, D.S.; Gienger, A. High-performance mount for the SOAR telescope project. *Proc. SPIE* **2000**, *4004*, 127–134. [CrossRef]
33. Smith, D.R.; Avitabile, P.; Gwaltney, G.; Cho, M.; Sheehan, M. Wind-induced structural response of a large telescope. *Proc. SPIE* **2004**, *5495*, 258–269. [CrossRef]
34. Noethe, L. Active optics in modern large optical telescopes. *Prog. Opt.* **2002**, *43*, 1–69. [CrossRef]
35. MacMynowski, D.G.; Vogiatzis, K.; Angeli, G.Z.; Fitzsimmons, J.; Nelson, J.E. Wind loads on ground-based telescopes. *Appl. Opt.* **2006**, *45*, 7912–7923. [CrossRef]
36. Zhang, J.C.; Ge, L.; Lu, X.M.; Cao, Z.H.; Chen, X.; Mao, Y.N.; Jiang, X.J. Astronomical Observing Conditions at Xinglong Observatory from 2007 to 2014. *Publ. Astron. Soc. Pac.* **2015**, *127*, 1292–1306. [CrossRef]